1992

Instantaneous structure of vortex breakdown on a delta wing

Joseph Towfighi
Lehigh University

AUTHOR:

Towfighi, Joseph

TITLE:

Instantaneous Structure of Tortex Breakdown on a Delta Wing.

DATE: January 17, 1993

INSTANTANEOUS STRUCTURE OF VORTEX BREAKDOWN ON A DELTA WING

by
Joseph Towfighi

A Thesis
Presented to the Graduate Committee
of Lehigh University
in Candidacy for the Degree of
Master of Science
in
Mechanical Engineering

Lehigh University
Bethlehem, Pennsylvania
December 1992

CERTIFICATE OF APPROVAL

This thesis is accepted and approved in partial fulfillment of the requirements for the degree of Master of Science.

12/01/92

date

Professor in Charge

Department Chairperson

To My Family and Friends

ACKNOWLEDGEMENTS

Now that the thesis is finished, I want to thank all the people who reminded me there is a time for everything. In order to accomplish this task a person needs to be balanced in many areas, and many times I find myself going to extremes, and the following are those who wisely decided to go along for the ride, or help me reevaluate my priorities, when necessary.

Family members - Mom, Dad, Joyce, Ursula, Rich, Brian

Thank you for your very much needed love and support.

Second family members - Maria, Gus, Anthony, Chris, Ryan, Orlando

You truly have accepted me into your family and that has helped me accomplish this goal.

Advisor - Professor Donald Rockwell

Thank you for your support and guidance. I truly appreciate the help you gave me, it has taught me many important lessons.

Lehigh Crew - Tim, Ozgur, Lin, Necati, Chyu, Kim, Jin, John, Chuck, Martin, Ned, Dave, Steve, Bill, Gary, Georg, Julie, Kim

Thanks people, sometimes extremes are necessary, and blue on white with silver is a comforting blend, that I will never forget. Without your help this paper would not be nearly as complete.

Drexel Crew - Coy, Serg, Ed, Kyle, Mike, Jenn, Pam, of course Debbie, and all my co-workers at Dyna East

Sometimes there is a strong need to get away from Bethlehem for a short period of time, thanks for providing that outlet.

Very Special Thanks - God and Angela

TABLE OF CONTENTS

LIST OF FIGURES

1. ABSTRACT

The flow past a delta wing, inclined at a high angle of attack, is examined using Particle Image Velocimetry (PIV). The overall objective is to experimentally determine the instantaneous velocity field, thereby gaining insight into the vortex breakdown phenomenon. The flow field is studied for times immediately following the pitching maneuver of a delta wing to an angle of attack of 40°. The transient motion of the onset of vortex breakdown from the trailing edge towards the apex, as well as unstable fluctuations about the quasi-steady state of vortex breakdown, are examined in detail.

Contours of constant vorticity and streamline patterns are obtained from the instantaneous velocity field, which in turn is determined in a plane passing through the centerline of the vortex core. In both the transient and quasi-steady state experiments, a switch in the sign of azimuthal vorticity exists just upstream of the position of the onset of vortex breakdown. Also, the general characteristics of the helical mode of instability of vortex breakdown are observed; time-dependent deviations from this mode occur; their relation to the bubble mode of vortex breakdown is unclear. Finally, values of circulation of the concentrations of vorticity, located just downstream of the onset of vortex breakdown, are calculated.

1. INTRODUCTION

The delta wing was first proposed for scientific study in the 1950's. Previously, research in aerodynamics had focussed on airfoil theory, in which the flow was assumed to remain attached to the wing's surface. As technology progressed and a greater understanding of lift and drag developed, the delta wing, which involved large-scale separation of flow from the leading-edge, became the most effective configuration for supersonic, high maneuverability aircraft. Most of the research on delta wings has been performed at low angles of attack. This introduction, however, will describe research pertaining to high angle of attack aerodynamics, for which vortex breakdown occurs upstream of the trailing-edge. This summary of previously related research will include a description of flow over the delta wing, and examine the concept of vortex breakdown.

1.1 DELTA WING CONFIGURATION

The general parameters, overall geometry and nature of the flow field associated with the delta wing will be described in order to provide a basis for understanding the phenomenon of vortex breakdown.

1.1.1 GENERAL GEOMETRY AND PARAMETERS

The planform view of the delta wing (figure 1.1) resembles a triangle. The angle of inclination, or sweep, of the leading-edge of the wing is defined by the sweep angle, Λ. The leading-edge is usually made sharp in order to provide the an essentially fixed line of flow separation. From the side view, the free- stream, U_∞, is inclined with respect to the wing at an angle, α, designated as the angle of attack. The chord length, C, is measured from the apex to the trailing edge along the centerline of the wing, and is the basic

length unit when determining the Reynolds number, Re_c. Usually, the thickness, t, of the delta wing is on the order of one-twentieth the length of the chord. The location of the onset of vortex breakdown, x_b, is measured with respect to the apex of the wing. Finally, delta wings are classified according to aspect ratio, $S = b^2/A$, where b is half the span of the base, and A is the planform area of the delta wing.

1.1.2 OVERVIEW OF FLOW FIELD

The flow over the delta wing results in large-scale leading-edge vortices. Figure 1.2 depicts a delta wing inclined at a low angle of attack α with respect to the direction of the freestream. The freestream flow incident upon the bottom surface of the wing is forced to turn outwards towards the edges of the wing, and separates from the leading-edge. At low angles of attack, the separated flow rolls inward, and forms a leading-edge vortex having a helical structure. Secondary vortex sheets of opposite rotation arise along the surface of the wing due to boundary layer separation. These primary and secondary vortex sheets extend downstream past the trailing edge of the delta wing.

1.2 CONCEPTS OF VORTEX BREAKDOWN

At a sufficiently high angle of attack known as the critical value, the flow undergoes a transformation near the trailing-edge of the wing. In this region, the flow in the leading-edge vortex changes from supercritical to subcritical, causing the vortex core to abruptly expand, corresponding to the onset of vortex breakdown. As the angle of attack is statically increased, the breakdown forms closer to the apex of the wing. This process continues until the angle of attack reaches fifty-five degrees (for a sweep angle of 75°), at which time the location of the critical point, signifying vortex breakdown position, reaches the apex of the wing, generating a condition of full dynamic stall above the surface of the wing.

1.2.1 MODES OF BREAKDOWN

The two major classifications of vortex breakdown were first discovered in flow over a delta wing at high angle of attack (Bryer and Lambourne, 1961). The first type of breakdown, portrayed in the bottom half of figure 1.3 (b), is called the bubble mode, due to the fact that the flow pattern seems to be axisymmetric, i.e. it appears as a body of revolution placed in the flow. The second type of breakdown known as the spiral mode is shown in the top half of figure 1.3 (b). The flow pattern is non-axisymmetric, and develops into a spiral configuration that rotates about the central core axis. At first it was thought that these two forms of vortex breakdown were just visual variants of the same flow state. For example, basing the breakdown only on its physical appearance can lead to the argument that the dye tracing the flow can be sufficiently deflected to resemble the spiral mode of vortex breakdown, if the local fluctuations near the stagnation points are strong enough. On the other hand these disturbances may be negligible for some flows, hence the physical deflections are imperceptible, and in turn the bubble form of breakdown is observed. However, two pieces of evidence have been noted from experimental observations that strongly controvert the previous viewpoint. First of all, the expansion of the breakdown core is larger for the bubble than the spiral, when undergoing the same flow stream conditions, thus suggesting that the two forms of breakdown are probably unique. The second piece of evidence is that the mean position of vortex breakdown for the spiral mode is always further downstream than that of the bubble mode for the same upstream flow parameters. These two experimental results tend to support the contention that the bubble and spiral modes are two distinct and separate forms of vortex breakdown (Leibovich 1978).

1.2.2 ONSET OF BREAKDOWN

The next aspect of vortex breakdown to be addressed is the location of the onset of vortex breakdown, referred to as the vortex breakdown position.

However, it should be understood that this position actually strays upstream and downstream of its mean location. One theoretical approach to predict the breakdown location in the flow involves comparing the vortex breakdown to a hydraulic jump (Benjamin, 1962). If the volumetric flow rate (Q) remains constant for a rectangular cross section of fluid with depth (h), mean axial velocity (u), and the gravitational constant (g), there are two possible states of uniform steady flow. The first state is termed supercritical, and occurs when the Froude Number (F):

$$F = u/(gh)^2 \tag{1}$$

is greater than one. The other state of flow is termed subcritical and occurs when the Froude Number is less than one. A property inherent to subcritical flow is that infinitesimal standing waves can be sustained throughout this region of the flow field, whereas in supercritical flow, these waves cannot exist. This result can be indicated by the solution of the following equation:

$$F^2 = \lambda/(2\pi h)\ \tanh\ (2\pi h/\lambda) \tag{2}$$

where λ, the wavelength of stationary sinusoidal waves is only real when the Froude Number is less than one, or when the flow is subcritical. A hydraulic jump occurs when the flow undergoes a sudden transformation from highly supercritical flow to the subcritical flow state. At this transitional site (figure 1.4) a large amount of turbulence, and an increase in the height of the flow, is noticed. Due to the increase in height, and a constant volumetric flow rate, the downstream velocity from this location is substantially decreased, when compared to the flow upstream of this location. This can be proven through the continuity equation, where:

$$v_2 = v_1 h_1/h_2 \tag{3}$$

and in turn the Froude number downstream of this location is less than one, indicating the subcritical flow state. This transition will not occur spontaneously, unless the Froude number is very close to one. In order for the transformation to occur, it needs a catalyst, such as an obstruction across the flow.

The next step in Benjamin's analysis was to assume the flow upstream of the vortex breakdown was supercritical, and the downstream flow was subcritical. Thus the actual location of the vortex breakdown would be at the

transition between the two flow states. In analogy with a hydraulic jump, which involves an increase in the height of the flow, vortex breakdown shows an expansion of the vortex core. Also, standing waves can only propagate along the flow downstream of the breakdown location, indicating that the flow is subcritical, while the flow upstream of this location is supercritical. This can be theoretically proven by considering a standing wave disturbance of the form:

$$\Psi = \phi(y)\sin(\gamma x + \nu) \tag{4}$$

Where

Ψ = Stream function; $\phi(y)$ = Potential function

$\gamma = (2\pi/\lambda)$; x = Distance traveled; ν = Kinematic viscosity

The stream function along with a perturbation modeled by the equation:

$$\Psi(x,y) = \Psi(y) + \varepsilon\Psi(x,y) \tag{5}$$

Where

ε = Magnitude of the perturbations of the stream function

is applied to a swirl flow through a cylindrical channel described by the following equations:

Swirl Velocity: $V(y)$ = Circulation/radius of swirl = $\Gamma(y)/r$

Axial Velocity: $W(y) = d\Psi/dy$; $I(y) = (1/2)\,\Gamma(y)^2$

This affects the stream function of the flow in the following manner:

$$\Psi_{yy} + (1/2y)\Psi_{xx} - (W_{yy}/W - I_y/(2y^2W^2))\Psi = 0 \tag{6}$$

After taking the respective derivatives of (4), substituting them into equation (5), and dividing out the sin term, the following equation results:

$$\phi_{yy} + \{(1/2y)\gamma^2 - W_{yy}/W + I_y/(2y^2W^2)\}\phi = 0 \tag{7}$$

For each solution of ϕ (ϕ_0, ϕ_1, ϕ_2, ...) to this equation a corresponding real eigenvalue of γ^2 (γ_0^2, γ_1^2, γ_2^2, ...) can be determined, where γ_0^2 is less than γ_1^2, which is less than γ_2^2 and so forth along the real axis. Now rewriting the fluctuating part of $\Psi(x,y)$ found in (5) in terms of the potential gives:

$$\Psi(x,y) = \Psi(y) + \varepsilon\,\phi(y)\,e^{(-\gamma x)} \tag{8}$$

Thus if $\gamma_0^2 > 0$, γ_0 is positive and all the rest of the γ's are also positive. Substituting this result into (8) indicates that as x increases, the disturbance part of the stream function $\varepsilon\,\phi(y)\,e^{(-\gamma x)}$ is damped, and eventually vanishes, thus indicating standing waves cannot propagate downstream in this flow state. This means that the flow is supercritical. On the other hand if $\gamma_0^2 < 0$, γ_0 is an imaginary number and the standing wave disturbance $\varepsilon\,\phi(y)\,e^{(-i\gamma x)}$ will propagate downstream, thus paralleling the subcritical flow state of the hydraulic jump. Therefore the critical point between these two flow states can be designated as the location of the onset of breakdown.

A drawback of Benjamin's theory is that it can only address the flow downstream and upstream of the breakdown position. This is due to the fact that he bases his theory on a flow without axial variations. It has lately been proven by Faler and Liebovich (1977) that the flow existing within the breakdown region undergoes axial velocity changes. This is due to the stagnation points that form along the central axis of the vortex core, and the regions of fluid recirculation that form within the breakdown core (figure 1.5). So Benjamin's theory works well in determining the actual location of the breakdown, but is unsuccessful at trying to characterize the flow in this region.

Instead of utilizing the classical approach formulated by Squire (1960) and Benjamin (1962) in which the location of the onset of vortex breakdown was found by considering perturbations to an initial stream function, Lopez and Brown (1990) acquire this information directly from the azimuthal component of vorticity. For their analysis the velocity components of the swirl flow are defined as the swirl velocity, v, and the axial velocity, w. The equations for the azimuthal component of vorticity (η) are as follows:

$$\eta = \alpha_0 \zeta_0 (\sigma_0/\sigma - \sigma/\sigma_0) \qquad \text{for } \eta_0 = 0,$$

$$\eta/\eta_0 = \sigma_0/\sigma(\alpha_0/\beta_0) - \sigma/\sigma_0(\alpha_0/\beta_0 - 1) \qquad \text{for } \eta_0 \neq 0 \tag{9}$$

Where:

η = Azimuthal component of vorticity

ζ = Axial component of vorticity

β = Helix angle of vorticity = $\tan^{-1}(\eta/\zeta)$

α = Helix angle of velocity = $\tan^{-1}(v/w)$

σ = Radius of stream surface

(All initial values are denoted with subscript zero. They are calculated at location z_0, as shown in figure 1.6)

From this equation, it can be observed that azimuthal vorticity downstream of z_0 depends only on the ratio of the helix angles of velocity to vorticity on the stream surface at z_0 and the ratio of the radius of the stream surface, σ, to the radius at z_0. Since the process of vortex breakdown involves a rapid expansion of the vortex core, the stream surface undergoes divergence thereby increasing the ratio σ/σ_0. Since the onset of breakdown is characterized by the occurence of a stagnation point along the axis of the vortex corresponding to a zero value of the axial velocity, w, there exists a relation between $w(0,z)$ and $\eta(\sigma,z')$:

$$w(o,z)=\frac{1}{2}\int_{-\infty}^{\infty}\int_{0}^{\infty}\frac{\sigma^2\eta(\sigma,z')}{[\sigma^2+(z-z')^2]^{3/2}}\,d\sigma\,dz' \tag{10}$$

This equation shows that there must in order for $w(0,z)$ to go to zero, since all other terms in the integral are everywhere positive. Therefore equations (9 and 10) indicate that vortex breakdown will occur only when the helix angle of the velocity is larger than the helix angle of vorticity on some stream surfaces. When breakdown occurs, η/η_0 decreases and eventually becomes negative as σ/σ_0 increased due to the core expansion.

Equation (9) can give further insight into the abrupt expansion of the vortex core. Once the azimuthal component of vorticity becomes negative, a negative velocity will develop along the axis. By simply applying the continuity equation to this situation, the stream surface radius will increase, which according to equation (9) will increase the magnitude of the negative

component of azimuthal vorticity. In turn, the negative velocity along the axis increases, and so on. This positive feedback cycle will continue until the stream surface reaches a maximum radial displacement, termed "overshoot", which induces an oscillation in the stream surface. As the magnitude of the overshoot increases, the resulting wavelength of the oscillation decreases, thereby increasing the probability for a second zone of recirculation. This zone would be characterized by a second switch in the sign of azimuthal vorticity from negative to positive, which would give rise to a positive acceleration of the velocity along the core axis.

When applying these concepts to the more complex model of the flow over a delta wing, the results are similar up to the first recirculation region. This means that the ratio of the helix angle of velocity to vorticity existing in the vortex core gives a strong indication of whether vortex breakdown will occur, and aids in determining the strength and location of it.

Other theoretical approaches postulated to characterize vortex breakdown such as hydrodynamic instability to nonaxisymmetric perturbations (Ludwieg 1961) and combining wave propogation theory along with hydrodynamic instability theory (Leibovich 1984) explain important physical mechanisms of vortex breakdown, but more research is needed to eventually bring these ideas together under one theory that satisfactorally describes all the essential features governing vortex breakdown.

1.2.3 HYSTERESIS

Hysteresis can be defined as the lag in response time of the vortex breakdown position, while the delta wing is undergoing dynamic motion (Magness, Robinson and Rockwell, 1989; Wolffelt, 1986; and Wedemeyer, 1982). This means that as the delta wing is pitching upwards at a constant rate, the breakdown position will be further from the apex than for the static wing at the same angle of attack (figure 1.7). On the other hand, as the angle of attack decreases, the breakdown position remains further downstream than the static case. Moreover, if the pitching motion is stopped, there will be a

time delay for the breakdown position to travel from its dynamic location to its normal static location for that particular angle of attack. This response time is categorized into two groups (Abtahi and Reynolds, 1987). The first is based on the condition for which the static breakdown location is downstream of the trailing-edge of the wing. The time delay for this regime is the order of the convective time scale, i.e. the chord C divided by the freestream velocity U_∞. The second group, for which the breakdown position is over the delta wing, involves the breakdown approaching its steady state asymptotically, (figure 1.8); the total response time is between ten and thirty convective time scales (C/U_∞). The inherent propagation speed of the vortex breakdown is therefore the major influence in determining the response time.

2. EXPERIMENTAL APPARATUS

All experiments were conducted in a water channel in the fluid mechanics laboratory. The major parts of the experimental system involved the rig for the delta wing, a camera-bias mirror arrangement for taking pictures of desired views of the flow field above the wing, and a lens-scanning mirror system that could position the laser sheet at any location in the test section of the channel. All these components will be fully described in the following subsections; first, however, the water tunnel system will be addressed.

2.1 WATER TUNNEL

The water tunnel used for experiments is located in Packard Lab, Room 174 of Lehigh University (figure 2.1). The tunnel consists of several components, each of which has a unique purpose. The first consists of a large reservoir into which the water is initially pumped, drastically reducing the flow speed of the water, thus alleviating the undesired effects of having the flow turn through an angle of ninety degrees before entering the reservoir. After settling down inside the large tank, the water is drawn through the system by a pump and passes through a 50.8 mm thick flow regulator honeycomb that extends over the entire width of the channel. The honeycomb structure reduces the energy of the large-scale eddies in the flow. Two thin screens are placed a few centimeters further downstream to aid in the reduction of the perturbations in the flow field. At this stage, the flow enters a smooth contraction in which the width of the channel decreases from 1.83 m to 0.92 m, thereby increasing the velocity of the flow. The main test section extends from this point for a distance of approximately 4.88 m. In order to allow the laser to pass through the bottom of the channel, and be able to view the experiments from the side of the channel, the walls and floor of the tunnel are constructed of optically-transparent plexiglass. All interior surfaces of the plexiglass were polished and smoothed to keep the boundary

layers as thin as possible. After the flow reaches the end of the test section, it enters another screen-honeycomb arrangement, which prevents disturbances from propagating upstream and affecting experiments. Finally, the flow comes to rest in another large tank at the opposite end of the channel, from which the water is recirculated to the initial reservoir via an underground pipe-pump system.

The flow speed of the water, through the test section of the channel, is controlled by a variable speed motor, which drives the axial flow pump. The variable flow speed in the sixteen foot test section ranges from 25.4 mm/sec to 228.6 mm/sec.

In order to keep the water clean, a second, smaller recirculation system continuously pumps the water through a very fine particle filtration system, thereby removing unwanted dirt. Also, bleach is added to the water to destroy any algae or mold from growing in the channel.

2.2 DELTA WING TEST RIG

The position of the rig in the test section was 1.30 m downstream from the end of the water tunnel contraction, in order to insure that the flow distribution in the channel was uniform and parallel with the walls and floor of the channel. Also, the top surface of the delta wing was located far enough from the walls, and from the floor and surface of the channel to prevent significant blockage effects, as shown in figure 2.2. The delta wing was held stationary by two sturdy support struts connected to a thick aluminum plate, which in turn was attached to two beam supports spanning the top of the channel. Since the support struts holding the wing needed to be immersed in water, they were constructed of brass, therefore preventing corrosion. Also, they were designed to be as thin as possible to reduce the disturbances created as the water flowed around them. Finally, the second, shorter support was angled thirty degrees relative to the first vertical support, thus increasing the stability of the rig. The supports were, therefore, rigid against bending moments and forces, induced by the flow past the wing-support arrangement.

2.2.1 DELTA WING SYSTEM

The end of the vertical support, which held the delta wing, branches off into two separate supports having a 3.18 mm gap between them (see figure 2.2). A brass gear having a 12.7 mm radius is located in this gap. The gear is directly connected to a post on the outside of each leg, which is attached to the mid-chord of the delta wing. Therefore, as the gear turns, the wing moves through the same angle of rotation, due to the direct link between the two members. The only shortcoming of the design is that the center axis of rotation of the wing is at the midpoint of the gear, and is not positioned on the wing itself. However, the two locations are in close proximity to each other. The wing is made of half-inch thick plexiglass, and has a chord length of 243 mm. The sweep angle, Λ, equals 75°, and the leading-edges are beveled at an angle of 40° to induce large-scale vortex shedding at the sharp edge. All the surfaces of the wing are polished. The aspect ratio, which defines the ratio of the semi-span squared to the planform area, equals 0.536.

2.2.2 COMPUMOTOR

In order to comply with the need to pitch the wing at different ramp rates, a Compumotor was securely stationed above the thick aluminum plate. A large hole was drilled in the plate, through which a brass drive chain connected the gear rotating the delta wing to an arrangement of sprocket gears attached to the Compumotor shaft. These sprocket gears were chosen and positioned with the objective that every time the shaft of the motor completed one turn, the wing only pitched through 22.5° of motion, or a 16:1 gear reduction ratio. The reason for this was to make the pitching maneuvers very continuous and smooth. The Compumotor already had sufficiently reliable positional accuracy, since every 1.8° rotation of the shaft was divided into 125 smaller separate microsteps. This fact, along with the gear reduction ratio of 16:1 means that the wing pitches through 0.0009° for every discrete

step of the motor, producing a very smooth motion. The Compumotor is driven by a Z-241 computer where software, named SFG, is used to generate the desired motion profiles. Another program called ALT (Magness, 1990) sent these profiles to an indexer. The indexer then proceeded to transform the hexadecimal values into pulsed control signals that the Compumotor could recognize and, in turn, perform the desired motion in a matter of milliseconds. Figure 2.3 gives a schematic of the open-loop Compumotor system.

2.3 CAMERA - BIAS MIRROR ARRANGEMENT

Once the rig was finalized, a proper method of viewing the flow past the wing needed to be developed. Since this thesis was interested in flows over delta wings at high angles of attack the camera would also have to be inclined at the same angle to view the flow field. The solution was an optical rail with grooves along its sides, and two carriers, which could separately house the camera and the bias mirror driver. These carriers could translate and fix to any position along the length of the rail by sliding in the grooves and tightening its grip once set, thus giving full freedom of motion for viewing the wing on the rail's axis; figures 2.4 and 2.5 portray the top and side views for this situation. The rail was then securely attached to an aluminum plate at the end of which was a hinge that was firmly fixed to an I-beam extending from the water tunnel. The hinge allowed the entire plate to traverse through 90° of motion; thus the field of view could encompass most of the flow field above the wing by having the same angle of inclination as the wing's angle of attack. At the other end of the plate was a chain that could be snugly fastened to a post once the desired camera angle was reached. Also, a small leg support was incorporated into the plate's design, that laid flush against the wall of the channel, keeping the camera system from rocking out of focus. The only drawback of the system was that it could only take pictures of planes parallel to the vectors of the freestream velocity. Therefore, looking down the centerline of the wing was fine, however when viewing a plane

spanning the center of the vortex core, and passing through the wing's apex, the previously mentioned system was not flexible enough. For this field of view, a stationary tripod, on which the rail could be firmly placed, was utilized; figures 2.6 and 2.7 portray the top and side views for this arrangement. The tripod gave vertical translation, along with rotational motion on all three axes, while the rail system added the horizontal motion, thus giving freedom of motion in any direction or angle of rotation. This solved the problem of monitoring the vortex core, however since the depth of field of the camera was so small, and so many angles were now involved, correct focussing of the camera was difficult. Therefore, special care had to be taken when setting up the alignment of the camera and wing, whenever the tripod system was used.

The camera used in the experiment was the NIKON F-4, and the lens was a Micro-NIKKOR 105 mm. The back of the camera and its bottom were flush against aluminum plates once it was fully tightened into place on the carrier to keep the camera's view totally parallel with the rail's axis. The bias mirror driver was housed between aluminum plates to decrease vibrations and to hold the scanner steady. The driver along with the CX-660 controller were purchased from General Scanning Inc.

The final piece of the system was the bias mirror. It was positioned on the driver shaft at a 45° angle directly in front of the view of the camera, thus allowing the camera to see into the water channel. A new mount was created to hook the mirror to the shaft, since the old one was unable to keep the mirror from slipping while the driver was in operation. The design modification was to use two set screws instead of a single set screw to fasten the mount to the shaft. This design minimized the slipping to well within tolerable levels for gaining accurate results. A more detailed description of the bias mirror and its function will be presented in the section on experimental methods.

2.4 OPTICAL TRAIN FOR LASER SCANNING-MIRROR SYSTEM

A Lexel laser stationed underneath the channel creates an intensely concentrated beam of blue light at a power level of approximately 2 Watts. The main objective of the lens system is to focus the beam into a laser sheet at the location in the test section of the channel where photos of the flow field are taken. Therefore the design must be flexible enough to allow the laser sheet to be moved easily along the entire length of the test section, parallel with fluid flow; however, movement transverse to the flow was, also, desirable. The other goal of the design is to rotate the sheet so that it can cut a plane either parallel with the flow direction, or perpendicular to the flow, and at all the angles in between. In order to accomplish this task, a large rectangular plate made of aluminum and having a thickness of 12.7 mm was constructed to slide along two circular rails spanning the length of the test section (figures 2.8 and 2.9). The laser beam crosses above the plate and hits the first turning mirror, which deflects the beam 90°. It then goes through a diverging-converging lens arrangement after which it passes through a singlet, all of which are fixed on top of the plate.

The next stage consists of a round rotating aluminum plate with a removable turning mirror at the center and a scanning rotating mirror at the outer edge. The beam first hits the turning mirror, and if set properly, is deflected directly into the rotating mirror. The mirror's outer circular face is constructed of 72 facets and is designed to spin continuously and at constant angular velocity. The beam hits a single facet at approximately a 45° angle and is deflected upwards towards the channel. Since the mirror is spinning, each facet forms its own individual laser sheet that appears continuous to the human eye, but is actually a single beam scanning in excess of 150 scans/sec and no greater than 14,000 scans/sec. The round rotating plate on which the rotating and turning mirror rests can slide along two rails that traverse the entire width of the channel, thus giving translational motion of the laser sheet perpendicular to the fluid flow. Also, the plate can be rotated, thus changing the angle of the laser sheet with respect to the direction of the freestream. If a laser sheet is desired that is transverse to the flow direction

the turning mirror is removed and the plate rotated so the beam travels directly into the rotating mirror. Finally, this arrangement of turning mirrors, lenses and rotating mirror, focuses the laser beam as it passes through the test section, thus resulting in the minimum diameter of the laser beam. The rotating mirror and its varying frequency motor controller were purchased from Lincoln Laser. For further information, the reader is referred to Corcoran (1992).

3. EXPERIMENTAL METHODS

The goal of this research is to obtain reliable and accurate measurements of the magnitude and direction of velocity vectors in a plane located above the delta wing, and intersecting the centerline of the leading-edge vortex. From these quantitative velocity data, streamlines, which are tangent to the velocity vectors, and vorticity, found by calculating the derivatives of the velocity vectors, can be determined. The technique known as Particle Image Velocimetry, or PIV, is the method used to obtain the planar velocity flow field. The PIV technique, along with the experimental design parameters, will be discussed in this section.

3.1 PARTICLE IMAGE VELOCIMETRY (PIV)

Over the years many advances have been made in the area of PIV, as described by Adrian (1991), Rockwell, Magness, Robinson, Akin, Gu, Corcoran, Towfighi (1992), and Rockwell, Magness, Akin, Corcoran, Towfighi (1992). The effective intensity of the laser sheet was increased, causing more light to be reflecteded by the particles; thereby, strengthening the exposed image on the film. Improving and optimizing the software and hardware allowed more accurate and reliable determination of the velocity vectors. Flows having instantaneous streamlines turning through angles greater than 90° could not be resolved initially; a method of biasing the flow was implemented for these cases. These experimental systems are described in the following subsections.

3.1.1 FORMATION OF LASER SHEET

In the traditional technique of laser illumination of particles, a single laser beam is spread out to form the laser sheet, thereby drastically decreasing its

intensity per unit area. For the techniques developed in our laboratories rotating/oscillating mirrors are used to deflect the laser beam, and thereby scan the single beam across the planar flow field, continuously recreating what appears to be a laser sheet. The primary advantage is that particles are illuminated as the single laser beam scans across the flow instead of all the particles being lit simultaneously by spreading the beam into a sheet. This technique allows the generation of a laser sheet with a higher effective intensity.

Two techniques of accomplishing this task are: oscillating a flat one-sided mirror, or rotating a thin cylindrical mirror with a specific number of flat facets machined onto its outer face. All laser deflecting surfaces must have a highly reflective coating and be very flat to insure that all of the beam is deflected in the same direction. Depending on the experimental parameters, the oscillating mirror may be better suited, but overall the rotating mirror has been proven to be more effective for particle image velocimetry. The first disadvantage of the oscillating mirror is that it scans the laser beam in both directions across the laser sheet. Even though the retrace time is comparably small to its normal scanning direction, it does create a smaller secondary particle image on the negative that results in undesirable background interference for PIV. This problem is bypassed by the rotating mirror, since it only rotates in one direction at a constant angular velocity enabling each flat facet to scan the beam across the planar flow field. Secondly, due to the fact that the oscillating mirror has to rock back and forth, it is unable to reach high frequencies, while the rotating mirror uses inertia to its advantage and can spin at large angular velocities. This capability is very useful, because all experiments with flows traveling through angles greater than 90° almost always need scanning frequencies only attainable by the rotating mirror, which will be explained later. However, the oscillating mirror does have some advantages. For example the width of the laser sheet can be easily controlled to include whatever portion of the planar flow field desired, while the angular width of the laser sheet from the rotating mirror remains fixed. Also, the rotating mirror cannot be used for flows with freestream velocity less than 1.5 in/sec, because its lowest scanning frequency of approximately

150 scans/sec is too fast. The oscillating mirror, on the other hand, works well at this level, since its range is between 20 and 250 scans/sec. For more details on the rotating mirror, refer to Corcoran (1992).

3.1.2 IMPROVING SOFTWARE AND HARDWARE

A major reason for improving the software and hardware involved with PIV system is to increase the success rate of interrogation. Interrogation is the term used to describe the procedure of determining velocity vectors from a negative, which contains many images in the form of micron-sized dots representing the reflected light from the particles. An appropriate definition for success rate is the percentage of accurate velocity vectors out of the total number of calculated vectors. If the success rate were to be 100% the interrogated flow field would have a value at every grid location; however noise, random error, and other problems reduce this percentage. A minimum acceptable level for the success rate is about 90%, but utilizing the following procedure enables PIV to operate as close to 100% as possible for each different experiment.

The first area for improving the success rate of PIV occurs before actual determination of the velocity vectors, and deals with selecting the parameters that optimize the quality of the negative for interrogation. Once the general parameters of the flow field are chosen, such as the appropriate field of view for the camera, and the magnitude of the freestream velocity, the best settings for the camera and rotating mirror can be determined. The main goal in gaining a high success rate is for the spacing between successive images of the same particle on the negative to be approximately 1/10 of a millimeter. Obtaining this result can be accomplished by selecting the correct scan rate for the rotating or oscillating mirror. This frequency depends on the average value of the flow velocity throughout the entire view seen by the camera and the magnification of the flow field by the camera lens. Since the mean flow velocity is unknown at the start of the experiment, a baseline frequency can be computed by using the freestream velocity divided by 1/10 of

a millimeter. The shutter speed of the camera is consequently arrived at by dividing the baseline scanning frequency by 5 and choosing the nearest shutter frequency at which the camera can operate, which insures the number of images of the same particle appearing on the negative is between 4 and 6. Five pictures are then taken of the flow at seven different f-stops between 2.8 and 22 inclusive, and the film is developed. The clearest picture of the flow is then used to measure the average distance between particles, thereby indicating the proper proportion for determining the optimal scanning frequency of the rotating mirror that would result in 1/10 millimeter spacing between particles on the negative. The new shutter frequency is then chosen by the method described above, and another series of pictures are taken over the previously mentioned range of f-stops. From this study, the highest f-stop that produces a clear image of the properly- spaced particles on the negative is deduced, and used for the rest of the experiments involving this particular field of view, unless the lighting in future tests changes. The reasons for choosing the highest f-stop possible are: focussing the camera is easier due to the larger depth of field; and the particles appear sharper and clearer, since the background is whiter, due to the higher contrast. Also, a strong contrast must exist between the particle images and the background of the negative, because as they approach equal levels, the background generates noise during interrogation comparable to the desired output level of the particle images, resulting in erroneous calculations of the velocity vectors. Once this parametric study is complete, proper settings for the camera and rotating mirror are known, and the negatives are optimized for interrogation.

The second area involves perfecting the software and effectively utilizing advanced digital scanning equipment to calculate velocity vectors much faster and more accurately directly from the negative. In order to explain the improvements, a brief description of the process of calculating the planar velocity flow field must be given. An optical Fast Fourier Transform (FFT) is performed on the picture by shining a laser beam, whose diameter is approximately 1 mm through the negative (figure 3.1). This beam is then focussed by a lens into a video camera, and the interference pattern of the particle images within a circle defined by the diameter of the laser beam is

directly digitized onto a 386 IBM personal computer with the aid of a program called PDV provided by Lourenco. Once the optical FFT is completed a second FFT is computed by PDV on the digitized fringe pattern, thus enabling the program to calculate the magnitude and direction of the velocity vector for that particular location on the negative. Next two mechanical arms, also controlled by the code, proceed to move the negative one step at a time on the x and y axes; the increments and boundaries of the motion are specified by the user at the beginning of PDV. Velocity vectors are therefore obtained at each location over the entire planar velocity field corresponding to the negative.

Recently better curve-fitting techniques, along with an expansion of the FFTs from 64 x 64 to 256 x 256, have been incorporated into PDV to increase the accuracy of the calculated velocity vectors. Also, better utilization of advanced array processors by the program along with the usage of mechanical arms with a quick response time allowed the total time of interrogation to be reduced to 2 hours. Finally, a parameter is set in the beginning of PDV, which allows the user to choose above what noise threshold a velocity vector should be discarded. This helps eliminate some of the errors associated with interpretation of correct and incorrect velocity vectors.

3.1.3 FLOW BIASING

An important feature of the PIV system addresses situations in which reverse flow occurs in the field of view. These flows, for which the streamlines turn through angles larger than 90° cannot be successfully interrogated by the methods previously described. The method utilized to overcome this problem is to add a constant bias velocity to all the particles viewed by the camera. Since the bias mirror is placed directly in front of the camera, rotating it adds a nearly constant bias to all the particles in the flow field with respect to the frame of reference of the camera. Since the frequency of the rotation is so low with respect to the shutter speed of the camera and the scanning frequency of the laser sheet, assuming the bias to be a constant over the entire flow field is a reasonable assumption. If the constant bias is

large enough, all of the particles in the entire flow field will appear to travel in relatively the same direction, thereby eliminating reverse flow and streamline turns in excess of 90°. At this point, as long as the dynamic range throughout the negative does not exceed the capabilities of the interrogation system, the entire flow field can be calculated. If the dynamic range is too large, the motion of the bias mirror can be controlled to resolve this problem by adjusting the amplitude and frequency of the saw-tooth function along with properly resetting the frequency of the laser scans and the camera parameters. Once a successful PIV interrogation is completed, the constant bias can be subtracted from all the velocity vectors by the use of the program V, and the result is an accurate representation of the instantaneous velocity flow field.

3.1.4 RESULTS OF PIV

At this point, with all the optimal settings, most of the negative will yield satisfactory velocity vectors, and the success rate should easily be above 90%. In some locations, where the noise level calculated by PDV was above the noise threshold preset by the user, the velocity vector is rejected. In other spots, where the noise level was too high for PDV to calculate the velocity correctly, but the value was still below the threshold parameter set in the beginning of PIV, the velocity vector needs to be deleted. This can be done by first running a program called CVPIV, which transforms the data file created by PIV into a readable format. This new file output by CVPIV is then read into a program called V, which displays all the velocity vectors with their proper directions and magnitudes. The user must then make a critical assessment of the file and delete the incorrect velocity vectors that escaped elimination through the use of the noise threshold parameter. In order for a vector to be deleted by the user, it must be totally inconsistent in either magnitude or direction with all the velocity vectors surrounding it. After satisfactorily cleaning the file, the percentage of velocity vectors left must be

over 90% of the entire initial grid to complete the final test for acceptance. For these experiments, the total grid size was 67 by 35 points totaling 2345 possible velocity vectors, so only 2110 velocity vectors needed to be correct. For the most part the success level for these experiments was around 97%, which clearly met the satisfactory level.

Once the raw data have been properly cleaned, it is ready for post-processing. The file is first bilinearly interpolated by a program called FILV to fill in the missing velocity vectors. FILV the smoothes every velocity vector within the entire grid by using a square grid of sixty four velocity vectors surrounding the vector being smoothed in order to decrease the noise level of the velocity field. This is done by using a Gaussian kernel, which decreases the effect of neighboring velocity vectors exponentially, as the distance from the vector being smoothed increases. A parameter, called the smoothing factor, is set by the user in FILV; it controls the rate the exponential term decreases. A large value, such as 2.5, flattens and widens the Gaussian curve, thereby giving more significance to vectors farther away, and has the effect of smearing the flow field. On the other hand, a lower value, such as 0.9, decreases the influence of the neighboring vectors in the smoothing process, and results in approximately the same noise level. A value, which seems to produce the best results by leaving the inherent characteristics of the flow field untouched, is 1.3.

After execution, FILV outputs three files. Two contain the X and Y velocity components, while the third file consists of the out of plane strengths of vorticity, at each location throughout the grid. The X and Y velocity components can be reloaded into V, and after selecting any spot in the flow field, the streamline passing through that point can be calculated. Also, the azimuthal vorticity data can be opened by SURFER and any scaler level of vorticity existing in the flow field can be displayed. SURFER first interpolates between grid points to determine all locations of the user specified scaler level of vorticity, and proceeds to fit a cubic spline curve with a tension factor of 0.1 to display the vorticity contour. Since the resolution level is on the order of the grid interval spacing, which is 0.5 mm, any small scale vorticity, encompassing an area smaller than 0.785 mm^2, should be disregarded. Also,

the data found within one grid spacing from the borders of the flow is not as reliable, since interpolation and smoothing is dependent on a smaller number of neighboring vectors within these regions. With the aid of these software tools, many complicated fluid flows can be sufficiently analyzed.

3.2 EXPERIMENTAL PARAMETERS AND PROCEDURE

In order to perform the experiments, motion profiles for controlling the delta wing were created; when executed by ALT, they would operate the Compumotor to pitch the wing through any angle, thereby allowing the experimenter to orient the wing at an angle of 0° before the start of any test to eliminate any errors resulting from hysteresis. In order to accomplish this task, motion profiles were developed that pitched the wing through the following angles of α: 5°, -5°, 15°, -15°, 25°, -25°, 40°, and -40°. Also, motion profiles of $\alpha \sim$ 1°, -1°, 2°, -2°, 3°, -3°, 4°, and -4° were written and utilized to fine tune the wing to its initial angle of attack condition of α = 0°. The non-dimensionalized pitch rate used for all motion profiles was:

$$A = \alpha U / (2C) = 0.15 \tag{11}$$

which is well within the dynamic range of the Compumotor. The only problem with the compumotor occurs at the start and end of the pitching motion, due to the fact that angular acceleration curves are continuous. At the start of the motion, the Compumotor accelerates from a non-dimensionalized pitch rate of 0.0 until it reaches a constant of 0.15, while it decelerates in the same manner at the end of the maneuver. The period of acceleration and deceleration are very small in magnitude compared to the entire period of motion, and therefore have very little effect on the flow over the delta wing. Also, since the acceleration and deceleration modes are similar in curvature but perform the exact opposite operation the overall angular displacement of the delta wing remains unchanged resulting in pitching the wing through the desired angle.

Before beginning an experiment, the height of the water in the channel and the freestream velocity are checked and maintained at 0.56 m and 50.8 mm/sec respectfully, thereby keeping all tests consistent. These values result in a flow rate through the test section of the channel of 0.026 m^3/sec and a Reynolds number of approximately 11,300 based on the chord length of the delta wing of 246 mm. The next step involved orienting the laser sheet through the center of the vortex core with the wing aligned at an angle of attack with respect to the freestream direction of 40°. The wing was pitched from 0° to 40° and allowed to remain stationary for 5 minutes to insure breakdown settled around its mean equilibrium position. Dye is then injected into the flow at the tip of the delta wing, which proceeds to be carried by the flow thereby displaying vortex core, indicating an angular displacement of the laser sheet equal to 12.3° off the centerline of the delta wing in order for the laser sheet to traverse the center of the vortex core. The laser sheet intersects the apex of the wing, and passes through the base of the wing at a distance of 41 mm measured normal to the centerline of the wing. The camera-bias mirror rig is also pitched 40° to keep keep the field of view parallel with the angle of attack of the delta wing, and rotated 12.3° to keep the view parallel with the laser sheet. The entire rig is then translated until the field of view encompasses 8% to 96% of the upper surface of the wing with respect to the apex, while the entire thickness of the wing is placed in the top portion of the picture to indicate a characteristic length scale. At this point it is very important to keep everything perfectly aligned, otherwise double images of particles or other focus and depth of field related problems occur.

After optimizing the field of view, the parametric study described in section 3.1.2 is utilized to determine the best settings for the camera and rotating mirror. Without the bias mirror, the frequency of the rotating mirror equals 150Hz, shutter speed and f-stop of the camera are 30Hz and 8 respectively. Adding the bias mirror increases the rotating mirror frequency to 300Hz and changes the shutter speed and f-stop of the camera to 60Hz and 5.6 respectively. A parametric study was then performed on the amplitude and frequency of the bias mirror to determine what combination of these two

variables results in proper displacement between successive particle images over the entire negative along with the elimination of all streamlines turning through angles in excess of 90°, thereby optimizing the interrogation process. The best results for success rate during the interrogation process occurred at a frequency of 8Hz and an amplitude of 0.04 Volts for the bias mirror.

Once the negative is interrogated, the magnification, M, and the physical resolution d_I/M can be computed. The physical diameter of the laser beam, that shines through the negative, is the interrogation window diameter, which is the resolution, d_I, and equals 1 mm. Therefore in order for the grid size ΔL to satisfy the Nyquist criterion or 0.5 d_I it was set to 0.5 mm. The physical length, L_p, of the delta wing in the freestream or horizontal direction within the field of view was 216.5 mm. Since there are 66 steps contained over the entire length, ΔL_p is L_p/number of steps or 3.28 mm/step. The magnification, M, can then be calculated as follows:

$$M = \Delta L/\Delta L_p = 0.5 / 3.28 = 0.152 \tag{12}$$

Therefore the effective physical resolution or d_I/M equals 6.58 mm.

Now that the desired field of view is clearly focussed upon, and all the parameters are determined, the experiments can be started. The wing is returned to the initial starting position of 0° angle of attack, and the flow speed in the water channel is increased to 200 mm/sec. The channel is then seeded with an adequate amount of metallic coated particles with an average diameter of 9 μm and a density of 2.6 gm/cm^3 manufactured by TSI Corp. The channel remains at this speed for a few minutes until the particles are evenly distributed throughout the channel, and then is returned to a velocity of 50.8 mm/sec. Due to the fact that the specific gravity of the particles is greater than 1.00 the pictures should be taken as soon as possible before the particles settle to the bottom, but at least 5 minutes should be allowed to pass to insure the freestream velocity is constant throughout the test section of the channel. Note that the settling of the particles is very slight over the field of view, thereby it does not effect the results of the experiment.

For the first experiment, the wing is pitched by ALT from 0° to 40°, and the vortex breakdown is allowed to reach its mean equilibrium position. After two minutes have passed the flow field is ready for experimentation. Two shots are then triggered by using a profile executed by ALT. It properly synchronizes the firing of the camera with the bias mirror ramp cycle, so that the first picture is unbiased, and a second later the next picture is biased. The schematic of the open-loop system to drive the camera and bias mirror in proper synchronization is shown in figure 3.2. The reason for the first unbiased picture is twofold. First of all when the camera has not been used the delay time to when the shutter opens is random, but for the second picture the camera has just been used and the delay time equals .046 μsec, and can therefore be correctly synchronized with the bias mirror. Also, an unbiased picture of the flow a second before the biased picture gives an indication of how the flow should conceivably appear when the bias is subtracted by the program V. This process is then repeated 9 more times at randomly spaced time intervals to insure that all flow fields are fully time independent of each other.

The second experiment involved pitching the wing from 15° to 40° at a non-dimensionalized pitch rate of 0.15 and taking a picture of the flow as soon as possible after the motion stopped and every second thereafter for an entire roll of film. The only difference between the field of view for this experiment, compared to the first experiment, is that it now encompasses 5% to 93% of the upper surface of the wing with respect to the apex, in order to see more flow near the apex. Once the view is correctly repositioned, the wing is first reset to a 0° angle of attack, and all the parameters are rechecked, along with properly reseeding the channel. The wing is then pitched from 0° to 15° and two minutes are allowed to pass to let the vortex breakdown settle down to its mean equilibrium position. The wing is then pitched from 15° to 40°, and an unbiased picture is taken 1 second after the wing ceased motion. Two seconds after the wing ceased motion the profile executed by ALT triggers a biased picture, and continues to run taking a biased picture for every second thereafter for a total of 33 biased pictures, the last one taken 34 seconds after the wing ceased motion.

4. EXPERIMENTAL RESULTS

Vortex breakdown was examined on the delta wing for two basic situations. First of all the wing was maintained stationary and the time dependent variation of the flow structure was analyzed. Second, the wing was subjected to a pitching motion, which was abruptly terminated at the final angle of attack; the transient relaxation of the flow was then studied. The results of these two experiments are described in the following sections.

4.1 VORTEX BREAKDOWN ON STATIONARY DELTA WING

The first experiment dealt with obtaining the instantaneous velocity flow field of vortex breakdown, of a stationary delta wing inclined at an angle of attack, $\alpha = 40°$. Sectional streamline patterns and contours of constant vorticity were generated from the instantaneous velocity data. Figures 4.1 and 4.2 show the sectional streamline patterns and the contours of constant vorticity, respectively, for two cases selected from ten successful interrogations with a time interval greater than five convective time scales ($5\ C/U_\infty$) between consecutive pictures.

The onset of large-scale divergence of the streamline patterns is observed to occur between one-fourth to one-seventh of the distance from the left side of the images, which approximately corresponds to 31.8% to 22.5% of the chord length referenced from the apex. This onset of streamline divergence is one possible interpretation of the onset of vortex breakdown. Downstream of this point, regions of reverse flow, indicated by a rolling-up of the streamlines, along with the formation of saddle points in the streamline patterns, represent a very complex and highly unsteady flow. The inherent unsteadiness of the flow can be demonstrated by observing the drastic changes of the two sectional streamline patterns displayed in figure 4.1. In image (a) the location of the onset of vortex breakdown is positioned further downstream, and the degree of streamline divergence downstream of the

onset of breakdown, i. e. the transverse extent of the separated zone, is larger relative to that of (b). Also, the sectional streamline pattern of image (b) seems somewhat more symmetrical with respect to the center of the vortex core; it branches into two separated regions of reverse flow shortly after the onset of breakdown, whereas in image (a) flow continues to cross the vortex axis well past the the onset of breakdown. The final observation pertains to the streamlines generated at the outer edges of the region of vortex breakdown: close to the surface of the wing and adjacent to the freestream. These streamlines appear to form a sinusoidal wave, in which an increase in the wavelength between consecutive peaks occurs as the distance from the onset of vortex breakdown increases. This characteristic will be further elaborated on later in this section.

Contours of constant vorticity for the two cases are shown in figures 4.2, in which the negative contours appear as dashed lines, while the positive contours are solid lines. These contours exhibit a pattern that exists in all ten cases. A switch in the sign of azimuthal vorticity was observed near the location of the onset of vortex breakdown, corresponding to the point where the streamlines exhibit the onset of large-scale divergence. Upstream of the onset of vortex breakdown, positive azimuthal vorticity resides closest to the surface of the wing, while the negative component occurs on the opposite side of the axis of the vortex core. Downstream of vortex breakdown, the reverse situation exists; with negative azimuthal vorticity residing near the surface of the wing. This switch in sign is consistent with the theoretical study of Brown and Lopez (1990), explained in the introduction. Figure 4.3 is a plot of the location of the onset of vortex breakdown for all ten cases determined by using the switch in sign of the azimuthal vorticity as the governing criterion. These locations fluctuate above and below a mean equilibrium position of the onset of vortex breakdown, indicated by a dashed line on the plot, and determined by calculating the average of the ten data points, which is equal to 28.8% of the chord length from the apex, or $X_b/C =$ 0.288. The standard deviation for these data points from the mean equilibrium position equals 1.19, which is another indication of the unsteadiness inherent to the flow, since the value is significantly large.

Another repeatable flow characteristic occurring just downstream of the onset of vortex breakdown involves an increase in the highest level of azimuthal vorticity, by a factor of 1.5 to 2. Along with this increase the azimuthal vorticity becomes organized into well-defined vortical clusters, which persist downstream for four or five concentrations of vorticity, until the pattern breaks down forming more complex structures.

Depending on the arrangement of the negative azimuthal vorticity clusters with respect to the positive vorticity concentrations, two unique modes seem to exist. The first mode seems to emulate the helical or spiral mode of vortex breakdown in which corresponding clusters of positive and negative vorticity on opposite sides of the axis of the vortex core develop into a staggered arrangement. The spiral mode is displayed in image (a) of figure 4.2 in which the sign of the first four vorticity clusters appearing just after the onset of vortex breakdown is negative, positive, negative, positive, respectively. A second situation, which still represents the spiral mode of vortex breakdown, sometimes occurs in which the sign of the first four vorticity clusters are positive, negative, positive, negative, however this pattern appeared less frequently. Image (b), on the other hand, displays a pattern in which the centers of corresponding positive and negative vortical clusters coincide at approximately the same position above the surface of the wing, thereby representing what seems to be a deviation from the helical instability mode, and could possibly be interpreted as the bubble mode of vortex breakdown.

Considering these observations with the streamline patterns for these two cases strengthens the argument that two distinctly different modes are occurring. Prior experimental evidence has been limited either to qualitative flow visualization, or to time-averaged quantitative measurements. These results suggest, when comparing the bubble mode to the helical instability mode, that the onset of vortex breakdown occurs further upstream, and the sectional streamline pattern is much more symmetrical with respect to the centerline axis of the vortex core, for the bubble mode. This observation is consistent with the sectional streamline patterns portrayed in figure 4.1. There is not enough information to conclude that the streamline pattern of

figure 4.1 (b), and the vorticity contours of figure 4.2 (b) represent the bubble mode of vortex breakdown. An interesting observation is that out of the ten examined cases, the pure helical instability mode appeared eight times, indicating that it is the more dominant mode of vortex breakdown for this particular experiment.

Superposition of the streamlines on the corresponding contours of constant vorticity, shown in figure 4.4, indicate that the switch in sign of azimuthal vorticity occurs just upstream of the location of the onset of vortex breakdown, which is consistent with the numerical simulation of Visbal (1992). Also, some of the rollups of the sectional streamlines do seem to form near locations of concentrations of vorticity; however, using only the streamlines would not provide adequate information to discern the locations of all vortical clusters. Even the centers of well-defined sectional streamline rollups did not always coincide with the exact centers of the azimuthal vorticity concentrations, but they were strong indicators of a vortical cluster. At this point, it is necessary to re-examine the aforementioned sinusoidal wave patterns governing the streamlines generated close to the surface of the wing and near the freestream, but still within the region of vortex breakdown. It appears the wavelength of oscillation of the streamlines increases at the same rate as the wavelength between consecutive concentrations of vorticity of the same sign in the downstream direction. Also, if a line is drawn normal to the surface of the streamline at the point were the streamline hits an amplitudal peak furthest from the center axis of the vortex core, the line coincides, for the most part, with the center of a vortical structure. Therefore sectional streamlines can provide important information, but without the contours of constant vorticity exact locations of the center of vorticity concentrations, along with the more complex disorganized structures further downstream from the location of vortex breakdown, would remain unknown.

Figure 4.5 shows a plot of the sectional streamline pattern and the contours of constant vorticity obtained from calculating the average velocity field from all ten cases. Although the vortex breakdown flow characteristic of large-scale divergence in the sectional streamline pattern at the location of

the onset of breakdown still occurs, most of the other dominant features, indicated by the well-defined concentrations of vorticity, and the rollups of streamlines, have been smeared out. In fact, without any previous information, the streamline pattern of the time-averaging process appears somewhat symmetrical about the center axis of the vortex core, and could be misconstrued as the bubble mode of vortex breakdown. The formation of azimuthal vorticity does not give any indication of a spiral mode, even though the helical pattern was the dominant mode appearing in eight out of the ten cases. Finally, the switch in sign of azimuthal vorticity would go unnoticed, since the smearing effect lowered the highest level of vorticity so drastically, that it eliminated all vorticity concentrations upstream of the onset of vortex breakdown. The reason for the significant amount of smearing is attributed to the fact that the central locations of the vorticity clusters as well as their circulation and degree of concentration vary with time. Therefore, the low frequency unsteadiness present in the region of vortex breakdown requires careful interpretation of the time-average characteristics.

4.2 VORTEX BREAKDOWN ON DELTA WING FOLLOWING CESSATION OF PITCHING MOTION

The second experiment dealt with obtaining the instantaneous velocity flow field of vortex breakdown, after it has ceased a pitching motion at a final value, $\alpha = 40°$, after starting from an initial angle of attack, $\alpha = 15°$. A trial of 33 images with a time interval of one second between consecutive pictures were shot, equaling a total time duration of 33 seconds, which is almost equal to seven convective time scales ($7\ C/U_\infty$). During this time period the position of the onset of vortex breakdown relaxed from near the trailing-edge of the wing towards the mean equilibrium position of 28.8% of the chord length from the apex, determined in the first experiment. Out of the thirty-three cases, three were chosen at dimensionless times ($t\ U_\infty/C$) of 0.41, 0.83, and 3.30 to represent the relaxation process, and their corresponding sectional

streamline patterns and contours of constant vorticity are shown in figures 4.6 and 4.7, respectively.

The streamline patterns in figure 4.6 all show the onset of large-scale divergence in the sectional streamline pattern at the location of the onset of vortex breakdown. The transverse extent of the separated zone is similar to the results obtained in the first experiment. Other observations consistent with the first experiment are: streamline rollups along with saddle points residing downstream of the onset of vortex breakdown; and streamlines at the outer edges of the region of vortex breakdown take the form sinusoidal waves, however, the pattern is not as evident as in the streamlines adjacent to the freestream.

Figure 4.7 shows the contours of constant vorticity for the three dimensionless times. Once again, a switch in the sign of azimuthal vorticity is observed in all the images just upstream of the location of the onset of vortex breakdown, therefore, the theoretical concept of Brown and Lopez (1990), also, can be applied during the transient relaxation process of vortex breakdown. Superposition of the streamlines and contours of constant vorticity, displayed in figure 4.8, indicate that streamlines alone do not contain enough information to determine the exact locations and strengths of concentrations of azimuthal vorticity.

The location of the onset of vortex breakdown as it varies in time during the entire transient relaxation process, determined by using the switch in sign of azimuthal vorticity as the governing criterion, is plotted in figure 4.9. During the initial stages of the transient motion, comparable to the first 1.5 convective time scales, vortex breakdown moves very quickly from the trailing-edge towards the apex of the wing. Over the next three convective time scales the location of the onset of vortex breakdown progresses towards and reaches the mean equilibrium position of $X_b/C = 0.288$, concluded from the first section of results, and indicated by a dashed line on the plot. In this region, the onset of breakdown begins to oscillate back and forth, and the period of oscillation is observed to be approximately 0.6 convective time scales. Once the mean equilibrium position has been reached at about 4.5 convective time scales after cessation of the pitching motion, the flow

assumes the same characteristics of the experiment described in the first section of results, a stationary delta wing inclined at an angle of attack, $\alpha = 40°$. The position of the onset of vortex breakdown begins to fluctuate above and below the mean equilibrium position at a standard deviation of 0.391, and a period of oscillation on the order of 0.6 convective time scales. A logarithmic curve fit was then made to all the data points; it is shown as a solid line on the plot. The curve indicates the rapid movement of the onset of breakdown during the initial stages, the gradual slowing down of the motion, and finally the onset of vortex breakdown approaching the mean equilibrium position asymptotically.

Other characteristics common to both the transient relaxation phase and the stationary wing case described in the previous section are: 1) the highest level of azimuthal vorticity increased by a factor of 1.5 to 2 downstream of the switch in sign of azimuthal vorticity, 2) two forms of the helical instability mode of vortex breakdown occur in which the signs of the vortical clusters downstream of the location of the onset of breakdown are positive, negative, positive, negative for one case, and negative, positive, negative, positive for the other case, and (3) forms of breakdown which are a deviation from the pure helical instability mode, i. e. corresponding positive and negative vorticity clusters reside at approximately the same position above the wing, also, occur. In this experiment, however, the different modes of breakdown can be analyzed more completely by calculating the absolute values of non-dimensional circulation, Γ, for the first four concentrations of vorticity immediately downstream of the switch in sign of vorticity. The reason this was not done in the first section was due to the fact that significant portions of the concentrations of vorticity closest to the surface of the wing were missing, thereby introducing too much error in the calculations. During the transient relaxation process, as the concentrations of vorticity approach the mean equilibrium position, the distance between the vortical clusters of vortex breakdown and the surface of the wing continually decreases, until the situation exists in which the circulation values are no longer reliable, which occurs at convective time scales larger than 3.3.

In order to plot non-dimensional values of circulation, an appropriate

choice of the characteristic length scale needs to be made as mentioned earlier in experimental methods section 3.1.4. Since the size of a vortical cluster decreases as they approach the mean equilibrium position, a similar trend in the characteristic length scale may be necessary. Now, draw two lines, one through the centers of the negative vortical clusters within the region of vortex breakdown, and the other connecting the centers of the positive vortical clusters. Next, draw a line between the first two lines that exactly bisects the angle created by the first two lines. Finally, draw four lines that are perpendicular to the bisecting line, with each line intersecting the center of one of the four concentrations of vorticity being analyzed. The characteristic length scale for each vortical cluster is then found by measuring the length, l, of the corresponding perpendicular line, which connects the centers of positive and negative vorticity concentrations, bounded by the first two lines drawn, and could be considered the diameter of the core of vortex breakdown at that particular location. In order to insure that nothing is left out, the corresponding results of non-dimensional circulation, in which the characteristic length scale is the chord, C, of the delta wing are also plotted.

Figure 4.10 is a plot of the absolute values of the non-dimensional circulation for the first four concentrations of vorticity downstream of the onset of vortex breakdown for the six helical instability cases formed during the transient relaxation period. In order to portray any type of correlation between the six cases, the helical instability mode needs to be broken down into two categories. The first category contains four out of the six cases in which the signs of azimuthal vorticity concentrations in consecutive order immediately downstream of the onset of breakdown are: (a) positive, negative, positive, negative. The second category occurs when the signs of vorticity clusters in consecutive order immediately downstream of the onset of breakdown are: (b) negative, postive, negative, positive. These plots indicate that the helical instability mode of vortex breakdown seems to be comprised of two distinctly different modes. When comparing the curves within a single category of the helical instability mode for either of the characteristic length scales, the correlation is high, because each family of curves exhibit very similar trends. However, comparing the two categories of

the helical instability mode, for the same characteristic length scale, a much weaker correlation is observed. For example, using the diameter of the core of vortex breakdown as the characteristic length scale, a sharp increase in non-dimensional circulation is noted between the first and second vorticity clusters, after which the magnitude of the non-dimensional circulation continues to decrease for the next two vorticity clusters in all six curves graphed in the two plots in parts (a) and (b) on the left side of figure 4.10, which indicates some positive correlation. However, the reason the correlation is weak is due to the fact that the slopes of the curves between consecutive vorticity clusters differ dramatically between the two categories of the helical instability mode, especially between concentrations of vorticity numbered 2 and 3. A somewhat similar assessment can be made for the cases on which the chartacteristic length scale is based on the chord length. Finally, for the most part, all plots show a decrease in the magnitude or strength of non-dimensional circulation as time increases for both categories of the helical mode instability.

The next step is to compare the non-dimensionalized circulation curves for the helical instability mode of vortex breakdown to the two cases that seem to deviate from this mode. Once again both characteristic length scales, the chord and the core diameter of vortex breakdown, are used. However, it was difficult to determine which vorticity concentration came first, since in the this undetermined mode corresponding vorticity clusters of opposite signs within the region of vortex breakdown, reside at approximately the same position. Therefore, the first four vorticity clusters located immediately downstream of the onset of bubble mode of vortex breakdown were first assumed to be negative, positive, negative, positive (part a of figure 4.11), and then positive, negative, positive, negative (part b of figure 4.11) in order to make direct comparisons with the helical instability mode. Examining corresponding plots of figure 4.10 and 4.11 show little if any correlation, therefore supporting the contention that two distinctly different modes of voortex breakdown are occurring. Also, unlike the two categories of the spiral mode of vortex breakdown, the two curves portraying the non-dimensionalized circulation values of the vorticity concentrations for this

undetermined mode do not follow a similar trend, in any of the plots in figure 4.11. Therefore, a complete assessment of this mode cannot be made; however, a mode of vortex breakdown, distinctly different than that of the helical instability mode, does seem to occur.

4. CONCLUSIONS

The principal findings of this research program are summarized in the following:

- This study is the first experimental characterization of the instantaneous structure of the vortex breakdown phenomenon. Use of the Particle Image Velocimetry (PIV) technique provides new insight into the instantaneous velocity field, streamline patterns, and vorticity distributions.

- Quantitative measurements of the type employed in this study are necessary to fully understand the complex flow structure inherent to vortex breakdown.
  - The pure helical instability mode of vortex breakdown can be realized by noting the staggered rollups of the sectional streamline patterns, as well as a similar arrangement of the concentrations of vorticity.
  - A deviation from the helical instability mode of vortex breakdown occurs when the concentrations of vorticity are no longer staggered, but reside at approximately the same location above the wing. Drastic differences in the streamline patterns, as well as little correlation between the values of circulation for the two cases, supports the argument that these are deviated modes from the spiral mode. These modes may or may not be related to the bubble mode of vortex breakdown.

- Observations of the location of the onset of vortex breakdown suggest several key features:
  - The switch in sign of the azimuthal vorticity, possibly, can be used as a criterion to determine the location of the onset of vortex breakdown, since it occurs just upstream of this location.
  - During the transient period, following the cessation of pitching motion, the location of the onset of vortex breakdown goes through two phases. The first phase involves rapid movement from the

trailing-edge towards the apex. In the second phase, the movement of the breakdown gradually levels off, and asymptotically approaches its mean equilibrium position.

- During the quasi-steady state period, the location of the onset of vortex breakdown fluctuates above and below the mean equilibrium position with a period of oscillation on the order of 0.6 convective time scales.

- Averaging all of the instantaneous velocity fields, corresponding to the stationary delta wing, results in a drastic smearing of the dominant instantaneous characteristics associated with vortex breakdown. This is attributed to the fact that the locations of the vorticity clusters, as well as their circulation, and degree of concentration, vary with time.

- Evaluation of the sign and strength of circulation for each of the vorticity concentrations suggests several interesting patterns:
  - If the helical instability mode is broken down into two groups, in which the signs of the first four concentrations of vorticity residing downstream of vortex breakdown are positive, negative, positive, negative, and negative, positive, negative, positive, these patterns are found to be repeatable within each group.
  - When examining the graphs representing the deviated mode (relative to the pure spiral mode of vortex breakdown), little to no correlation is found between the curves within each group.

REFERENCES

Adrian, R. J., 1991, "Particle-Imaging Technique for Experimental Fluid Mechanics", Annual Review of Fluid Mechanics, Vol. 23, pp. 261-304.

Benjamin, T. B., 1962, "Theory of the Vortex Breakdown Phenomenon", Journal of Fluid Mechanics, Vol. 14, pp 593-629.

Brown, G. L., and Lopez, J. M., 1990, "Axismmetric Vortex Breakdown. Part 2. Physical Mechanisms", Journal of Fluid Mechanics, Vol. 221, pp. 553-576.

Corcoran, T., 1992, "Control of the Wake from a Simulated Blade by Trailing-Edge Blowing", M. S. Thesis, Department of Mechanical Engineering and Mechanics, Lehigh University, Bethlehem, Pennsylvania.

Escudier, M., 1988, "Vortex Breakdown: Observations and Explanations", Progress in Aerospace Science, Vol. 25, pp. 189-229.

Faler, J. H., and Leibovich, S., 1978, "An Experimental Map of the Internal Structure of a Vortex Breakdown", Journal of Fluid Mechanics, Vol. 86, Part 2, pp. 313-353.

Hall, M. G., 1972, "Vortex Breakdown", Annual Review of Fluid Mechanics, Vol. 4, pp. 195-218.

Harvey, J. K., 1962, "Some Observations of the Vortex Breakdown Phenomenon", Journal of Fluid mechanics, Vol. 14, p. 585.

Kegelman, J. T., and Roos, F. W., 1989, "Effects of Leading Edge Shape and Vortex Burst of the Flow Field of a 70-Degree-Sweep Delta Wing", AIAA Paper No. 89-0086, AIAA 26th Aerospace Sciences Meeting, Reno, Nevada, 9-12 January.

Lambourne, N. C., and Bryer, D. W., 1961, "The Bursting of Leading-Edge Vortices: Some Observations and Discussions of the Phenomenon", R&M 3283, Aeronautical Research Council.

Leibovich, S., 1978, "The Structure of Vortex Breakdown", Annual Review of Fluid Mechanics, Vol. 10, pp. 221-246.

Leibovich, S., 1984, "Vortex Stability and Breakdown: Survey and Extension", American Institute of Aeronautics and Astronautics Journal, Vol. 22, No. 9, pp. 221-246.

Ludwieg, H., 1961, "Contribution to the Explanation of the Instability of Vortex Cores Above Lifting Delta Wings", Aero. Versuchsanstalt, Gottingen, Rep., AVA/61, A 01.

Magness, C., Robinson, O., and Rockwell, D., 1989, "Control of Leading-Edge Vortices on a Delta Wing", AIAA Paper No. 89-0999, AIAA 2nd Shear Flow Conference, Tempe, Arizona, 13-16 March.

Payne, F. M., Ng, T. T., and Nelson, R. C., 1987, "Experimental Study of the Velocity Field on a Delta Wing", AIAA 19th Fluid Dynamics, Plasma Dynamics and Lasers Conference, 8-10 June.

Reynolds, G. A., and Abtahi, A. A., 1987, "Instabilities in Leading-Edge Vortex Development", AIAA Paper No. 87-2424, AIAA Applied Aerodynamics and Atmospheric Flight Mechanics Conference, Monterey, California, 17-19 August.

Rockwell, D., Magness, C., Robinson, O., Towfighi, J., Akin, O., Gu, W., and Corcoran, T., 1992a, "Instantaneous Structure of Unsteady Separated Flows Via Particle Image Velocimetry", PI-1 Report, Lehigh University, Bethlehem, Pennsylvania.

Rockwell, D., Magness, C., Towfighi, J., Akin, O., and Corcoran, T., 1992b, "High Image-Density Particle Image Velocimetry Using Laser Scanning Techniques", Lehigh University, Bethlehem, Pennsylvania, Sub. for Pub. in Experiments in Fluids.

Rockwell, D., and Towfighi, J., 1992, "Instantaneous Structure of Vortex Breakdown on a Delta Wing Via Particle Image Velocimetry", Lehigh University, Bethlehem, Pennsylvania, Sub. for Pub. in AIAA Journal.

Sarpkaya, T., 1974, "Effect of Adverse Pressure gradient on Vortex Breakdown", AIAA Journal, Vol. 12, pp. 602-607.

Squire, H. B., 1960, "Analysis of the Vortex Breakdown Phenomenon", Technical Report 102, Imperial College.

Wedemeyer, E., 1982, "Vortex Breakdown", AGARD Lecture Series No. 121, High Angle-of-Attack Aerodynamics, pp. 9-1 to 9-17.

Wolffelt, K. W., "Investigation of the Movement of Vortes Burst Position with Dynamically Changing Angle of Attack for a Schematic Delta Wing in a Water Tunnel with Correlation to Similar Studies in Wind Tunnel" AGARD CPP-413.

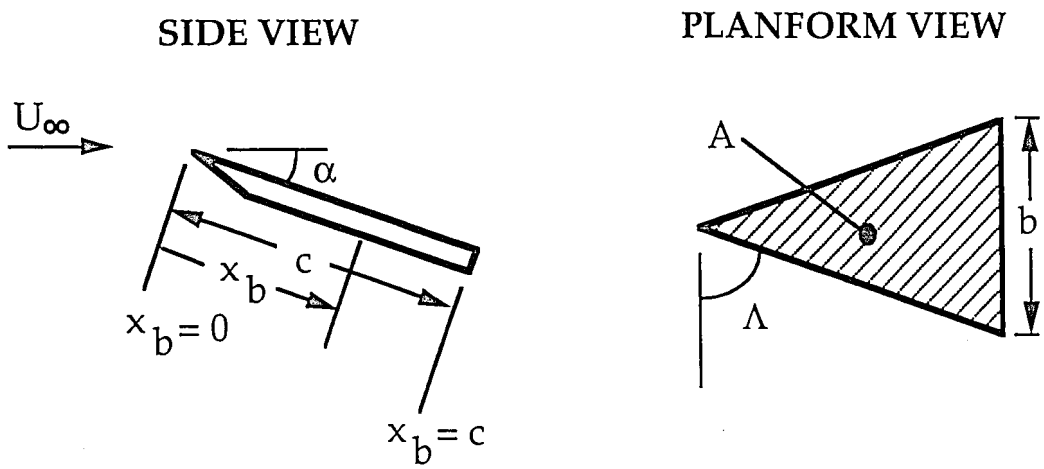

U_∞ - Freestream Velocity (in/sec)

c - Chord Length (in)

b - Trailing-Edge Length (in)

x_b - Breakdown position (in)

A - Area of Planform (in^2)

Re_c - Reynolds Number = $\frac{U_\infty c}{\nu}$

Λ - Sweep Angle (deg)

α - Angle of Attack (deg)

$\dot{\alpha}$ - Pitch Rate of Wing (rad/sec)

S - Aspect Ratio = $\frac{b^2}{4A}$

Figure 1.1 Delta wing parameters.

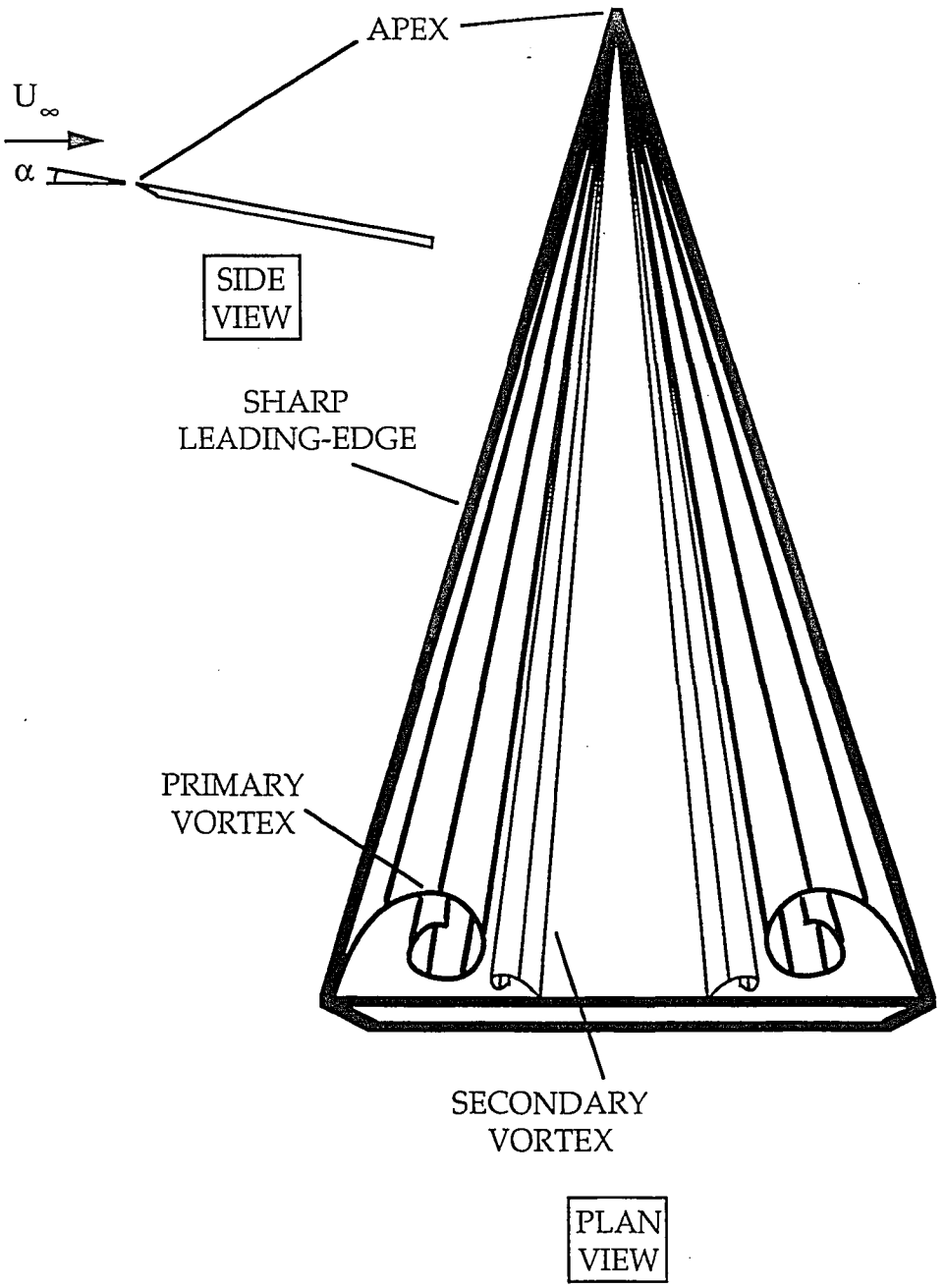

Figure 1.2: Flow over a delta wing inclined at a low angle of attack, α, with respect to the freestream.

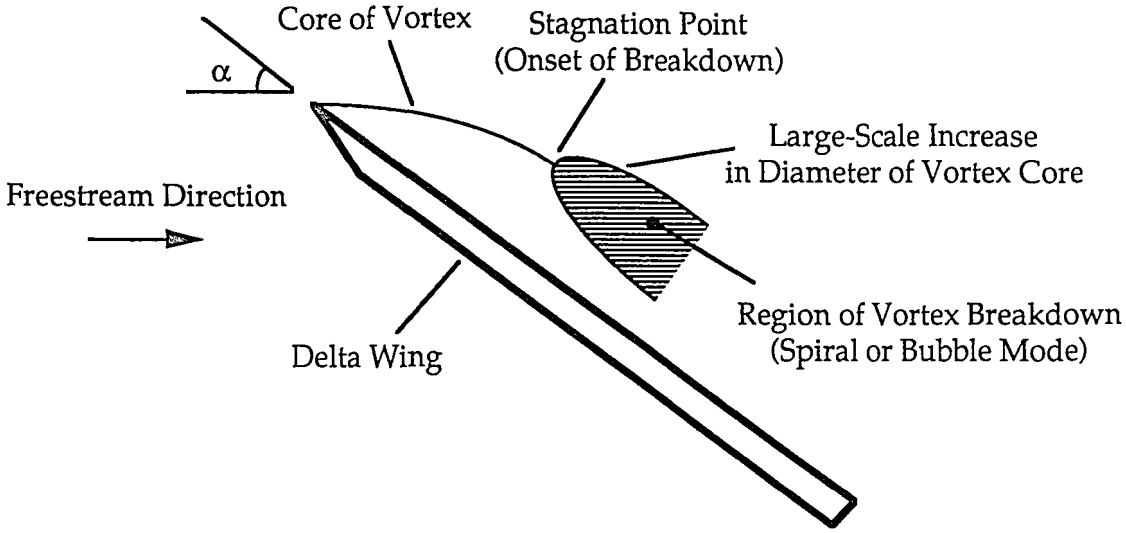

(a)

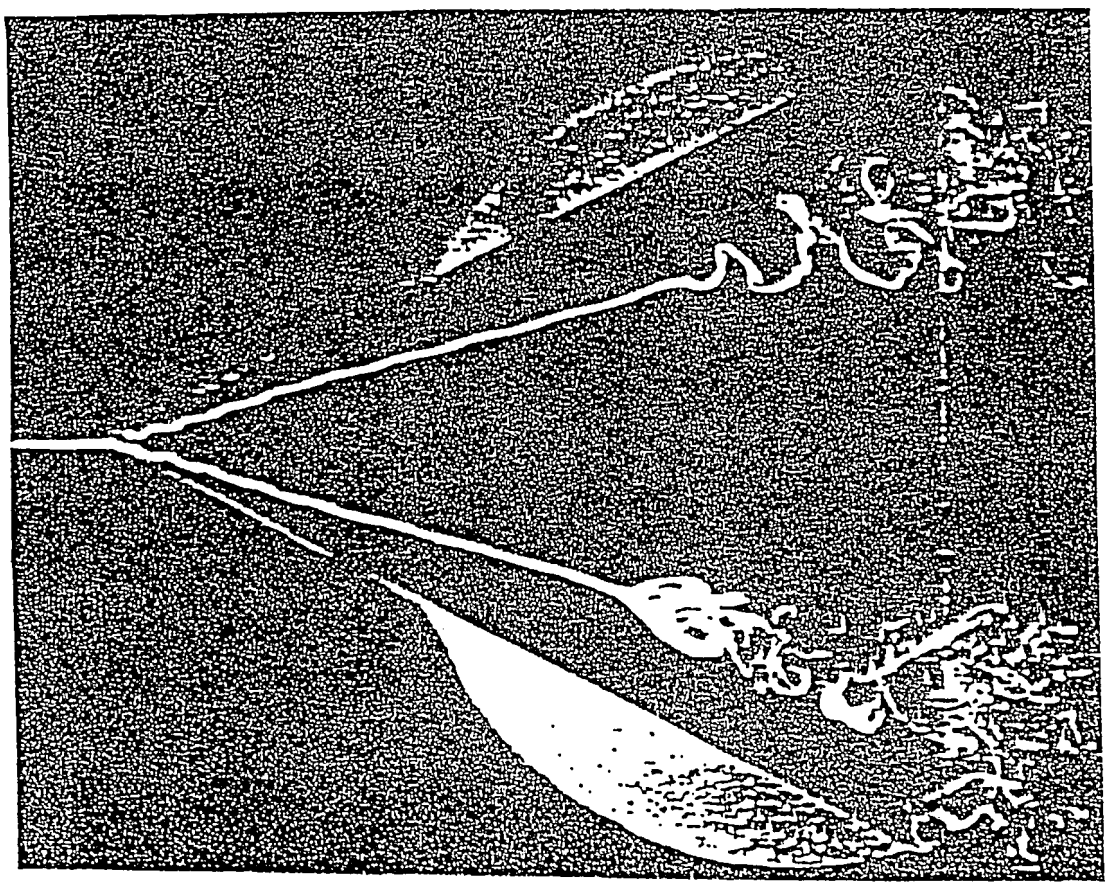

(b)

Figure 1.3: Vortex flow over a delta wing at high angle of attack portraying: (a) a side-view of vortex breakdown; and (b) the plan view of bubble and spiral modes of breakdown (From Bryer and Lambourne, 1961).

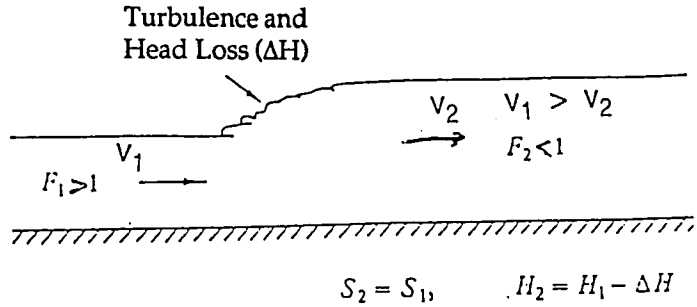

Figure 1.4: Steady flow undergoing the transition from supercritical to subcritical flow (From Benjamin, 1962).

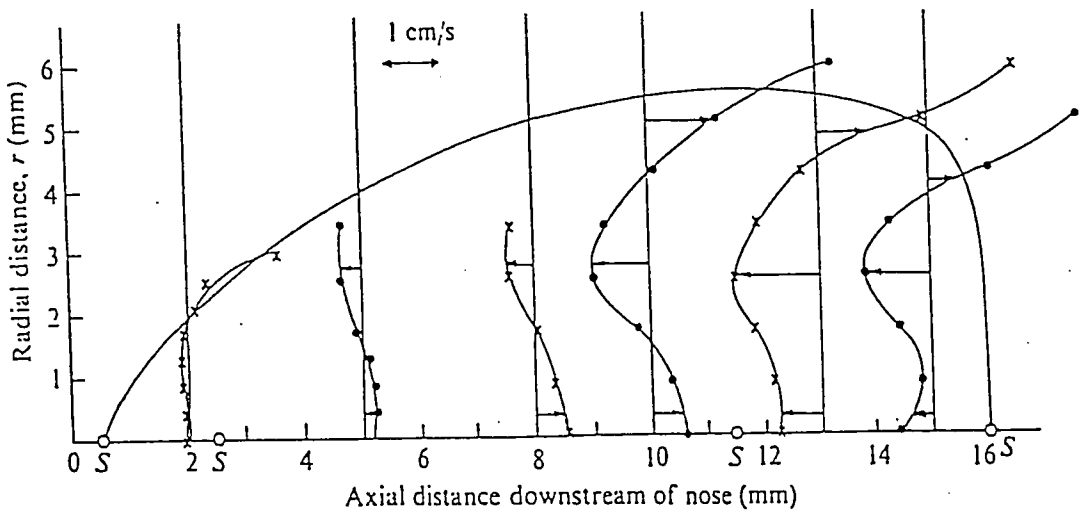

(a)

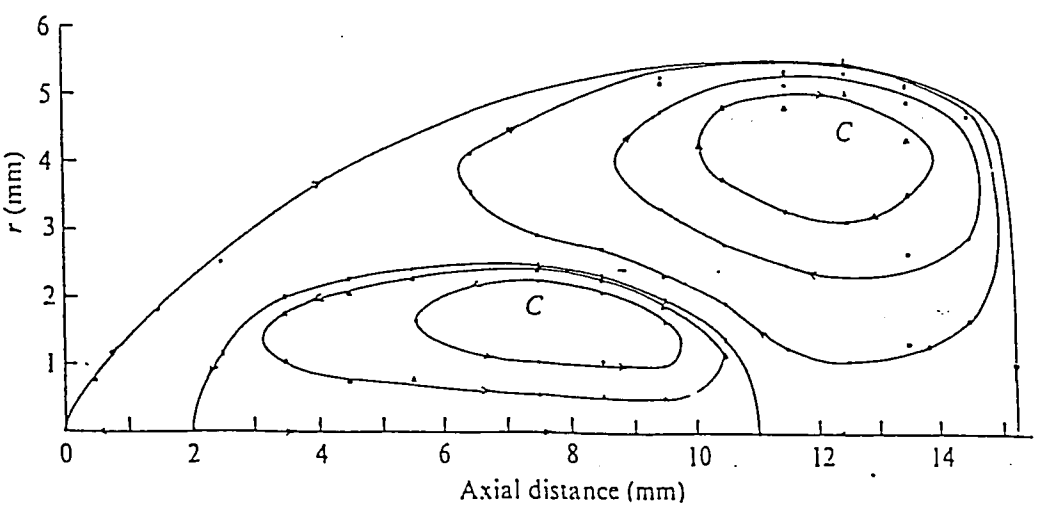

(b)

Figure 1.5: A map of the internal structure of the bubble mode of vortex breakdown showing (a) mean axial velocity profiles (S denotes stagnation point) (b) mean streamline patterns (C denotes center of recirculation zone) (From Faler and Leibovich, 1977).

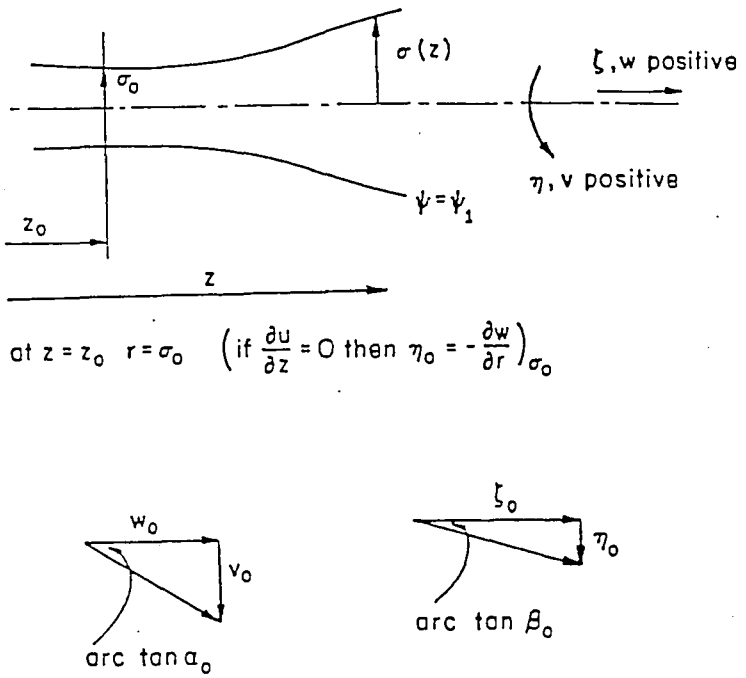

(a)

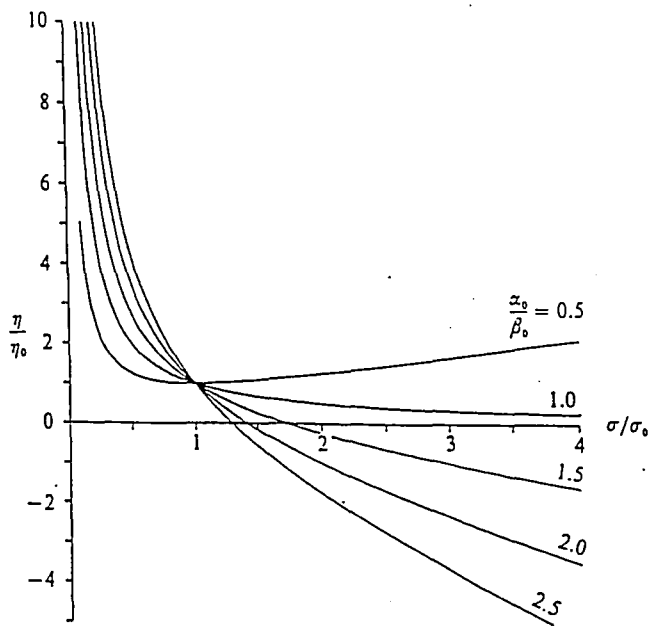

(b)

Figure 1.6: The coordinate system used on a stream surface (a) to set the initial helix angles, α_0 for the velocity, and β_0 for the vorticity, at z_0, along with the sign conventions for the variables; and (b) a plot of non-dimensional azimuthal vorticity, η/η_0, for various values of α_0/β_0. (From Brown and Lopez, 1990).

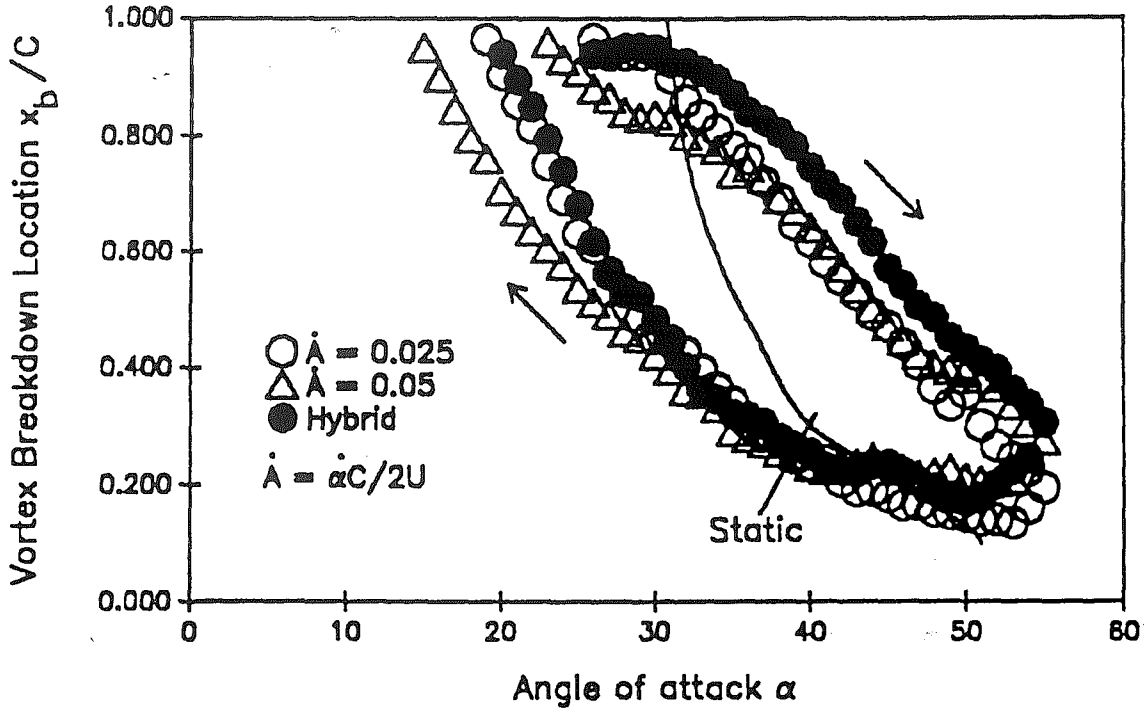

Figure 1.7: Breakdown position versus angle of attack for various pitching rates (From Magness, Robinson and Rockwell, 1989).

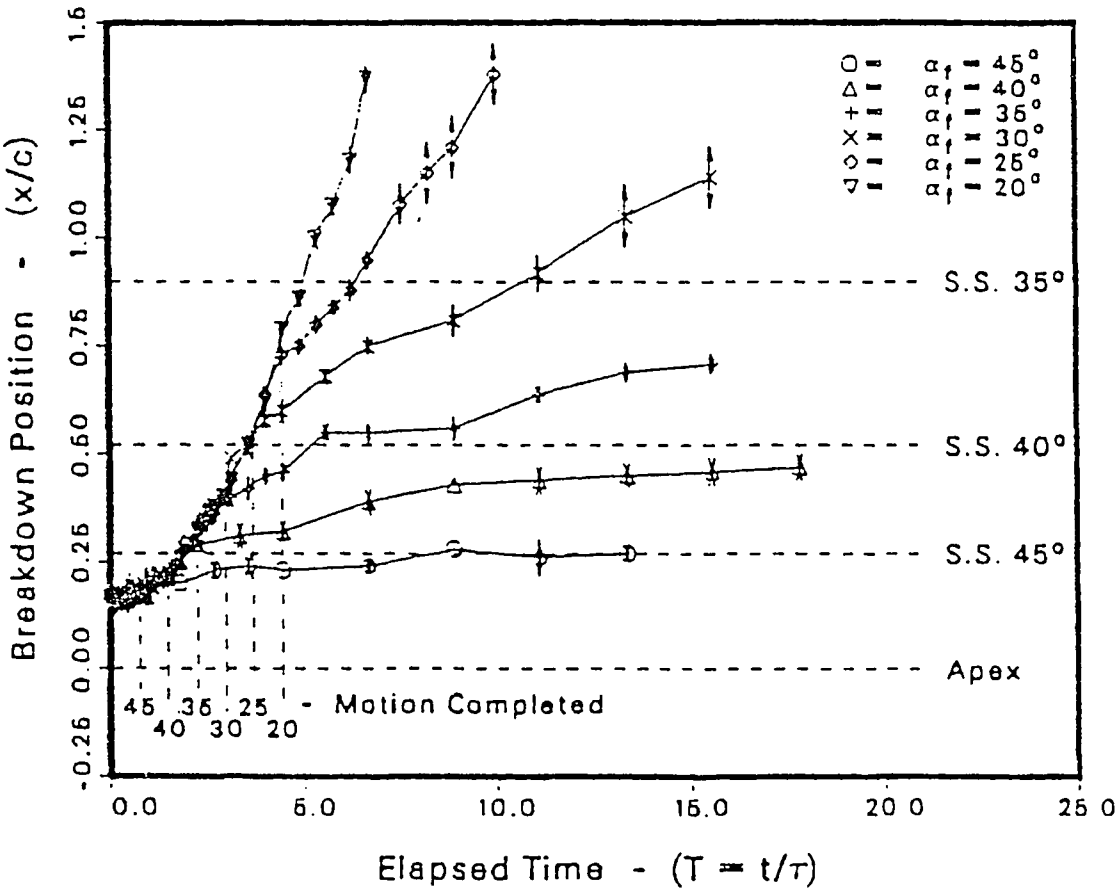

Figure 1.8: Behavior of vortex breakdown approaching its final steady state value after completion of motion from an initial angle of attack of fifty one degrees (From Reynolds and Abtahi, 1987).

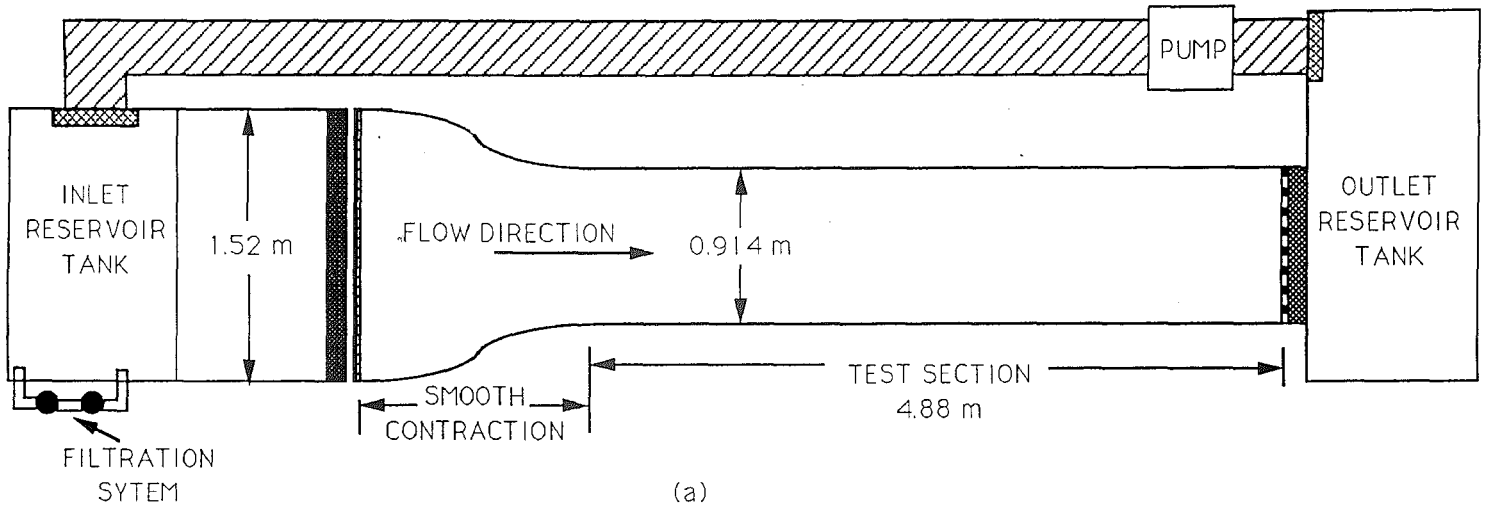

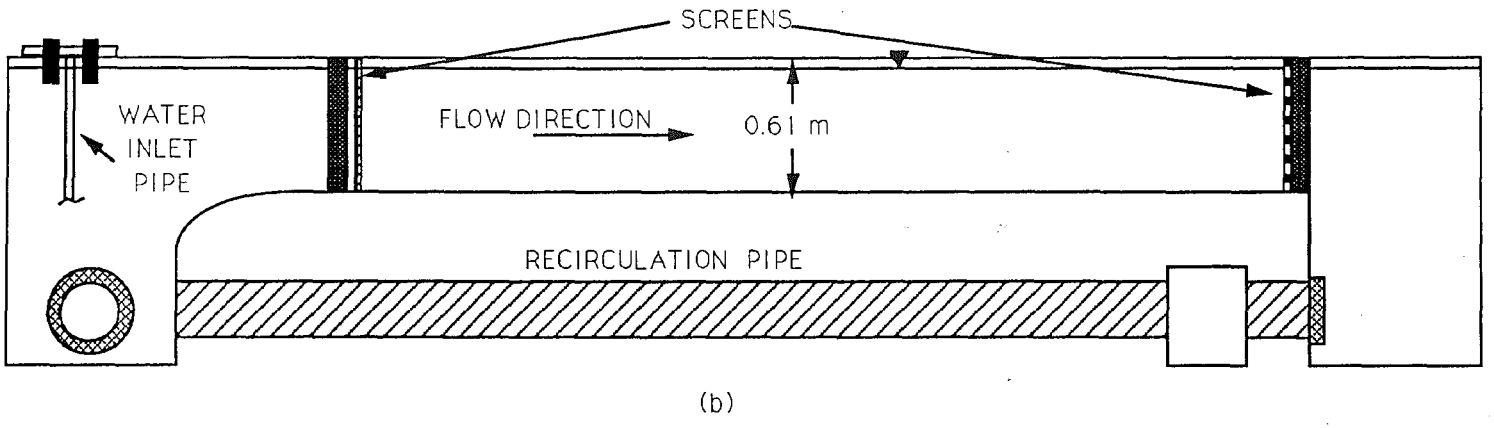

Figure 2.1: (a) Plan; and (b) side views of the water tunnel.

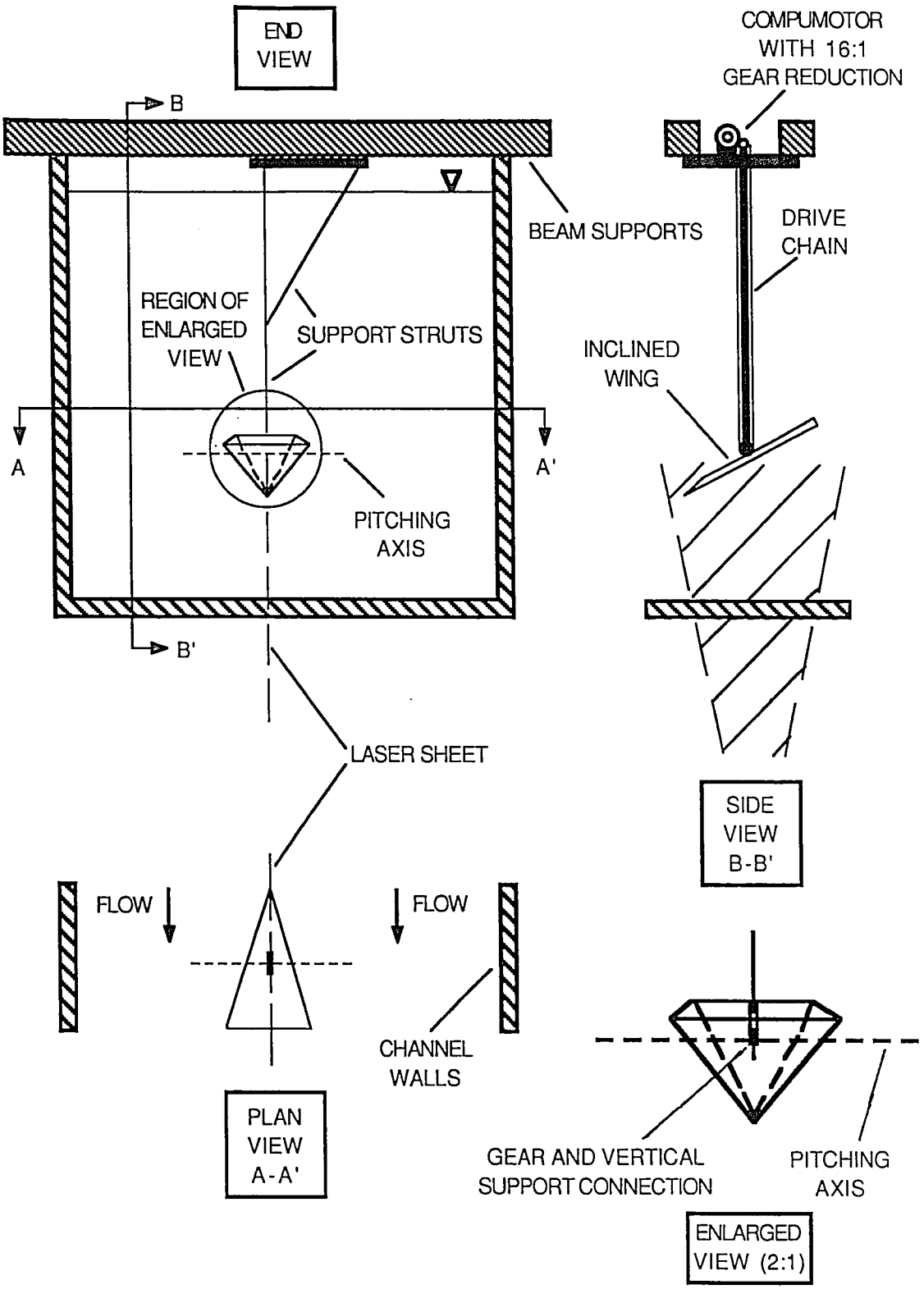

Figure 2.2: Plan, side, end, and enlarged views of the delta wing test rig.

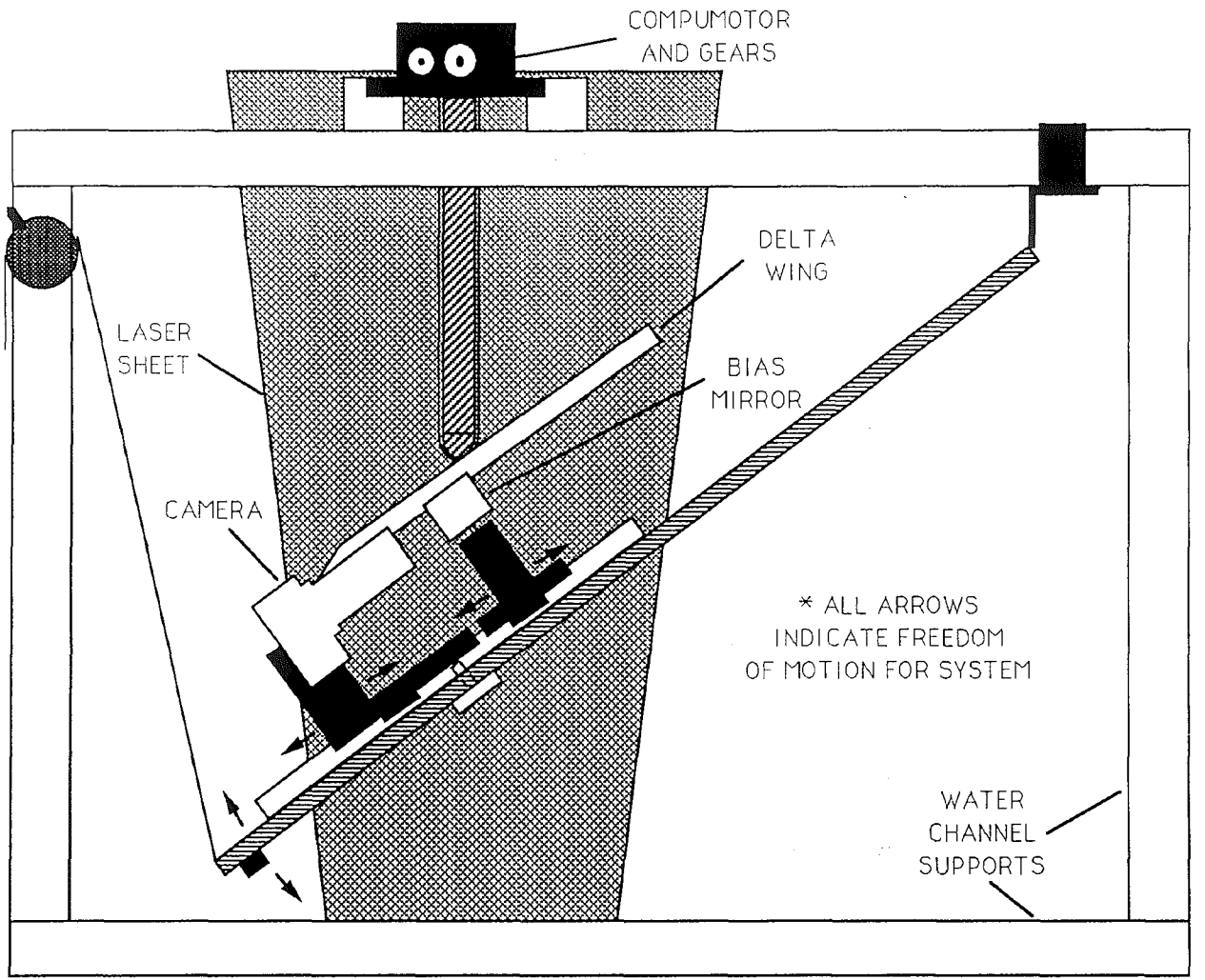

Figure 2.4: Side view of bias mirror and camera rig for viewing flow along center plane of delta wing.

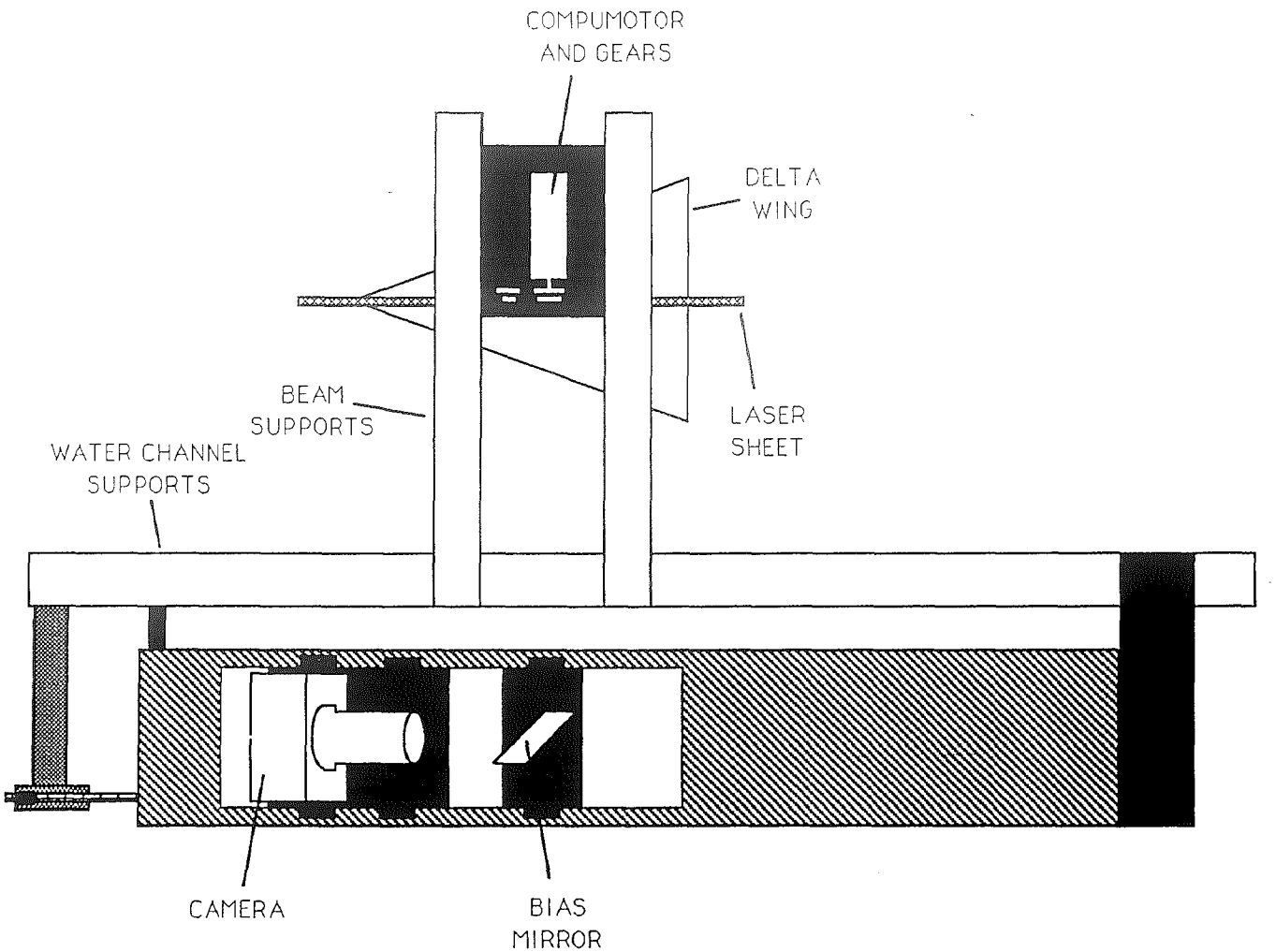

Figure 2.5: Plan view of bias mirror and camera rig for viewing flow along center plane of delta wing

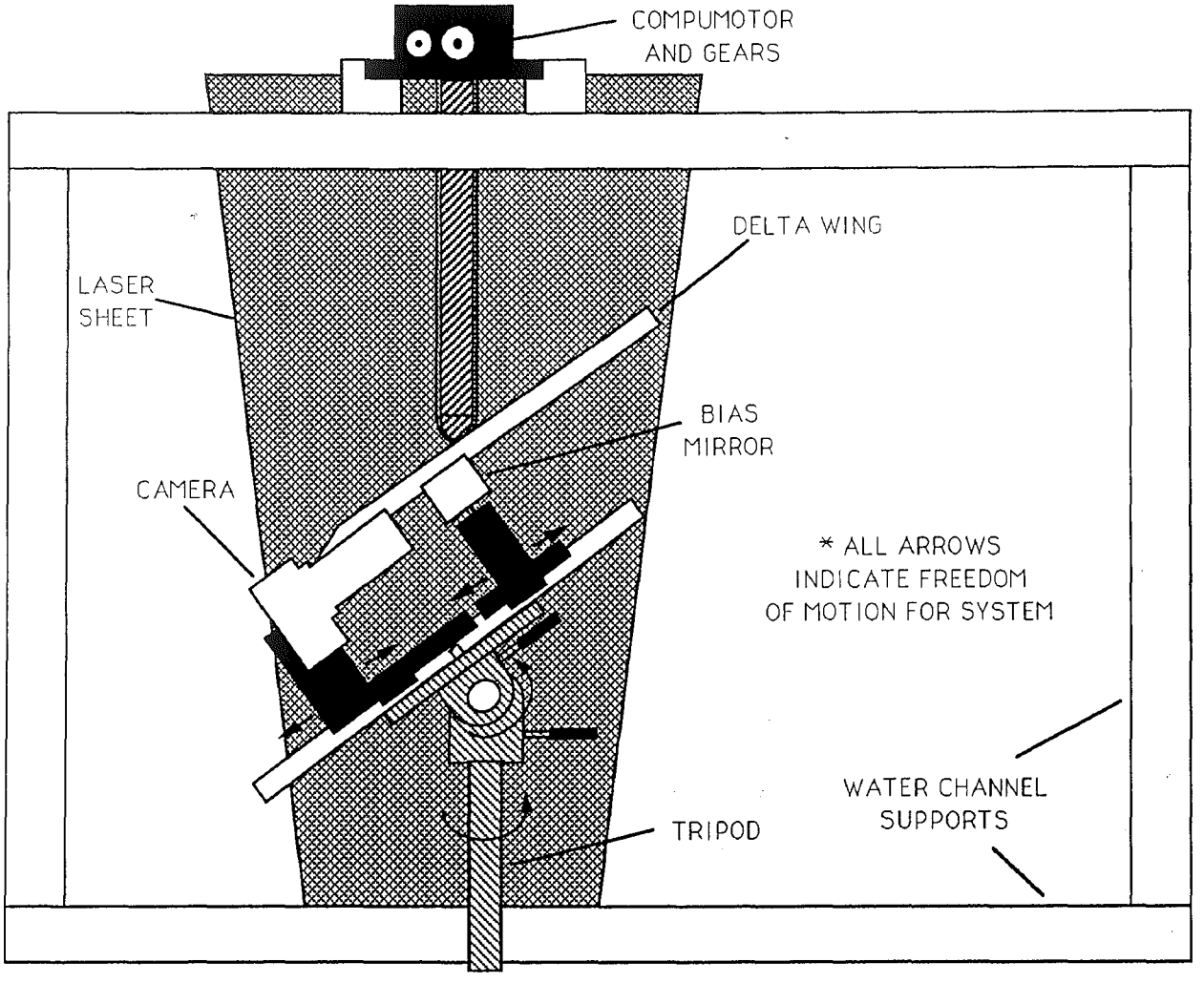

Figure 2.6: Side view of bias mirror and camera rig for viewing flow with plane passing through the centerline of the leading-edge vortex on the delta wing.

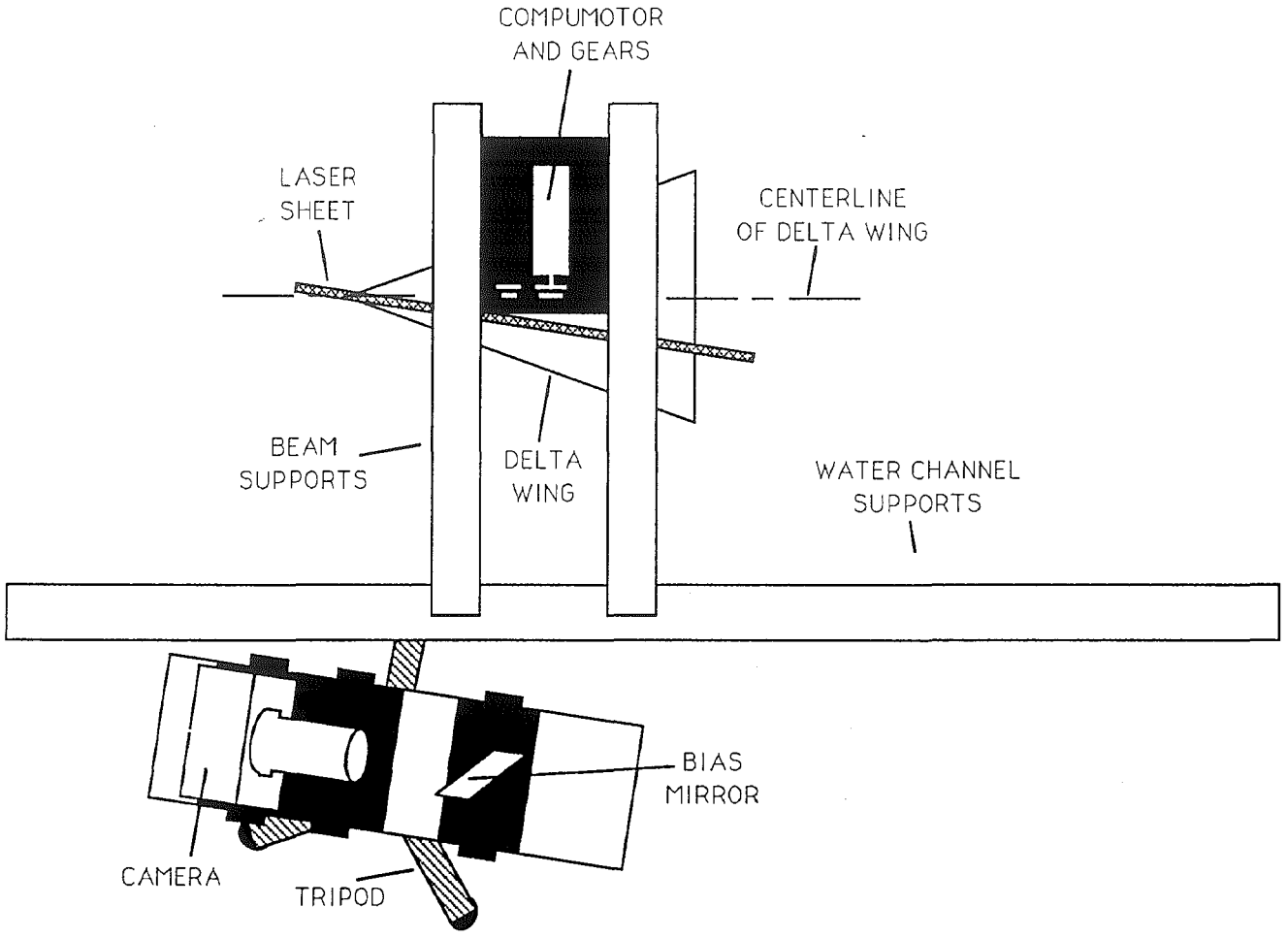

Figure 2.7: Plan view of bias mirror and camera rig for viewing flow with plane passing through the centerline of the leading-edge vortex on the delta wing.

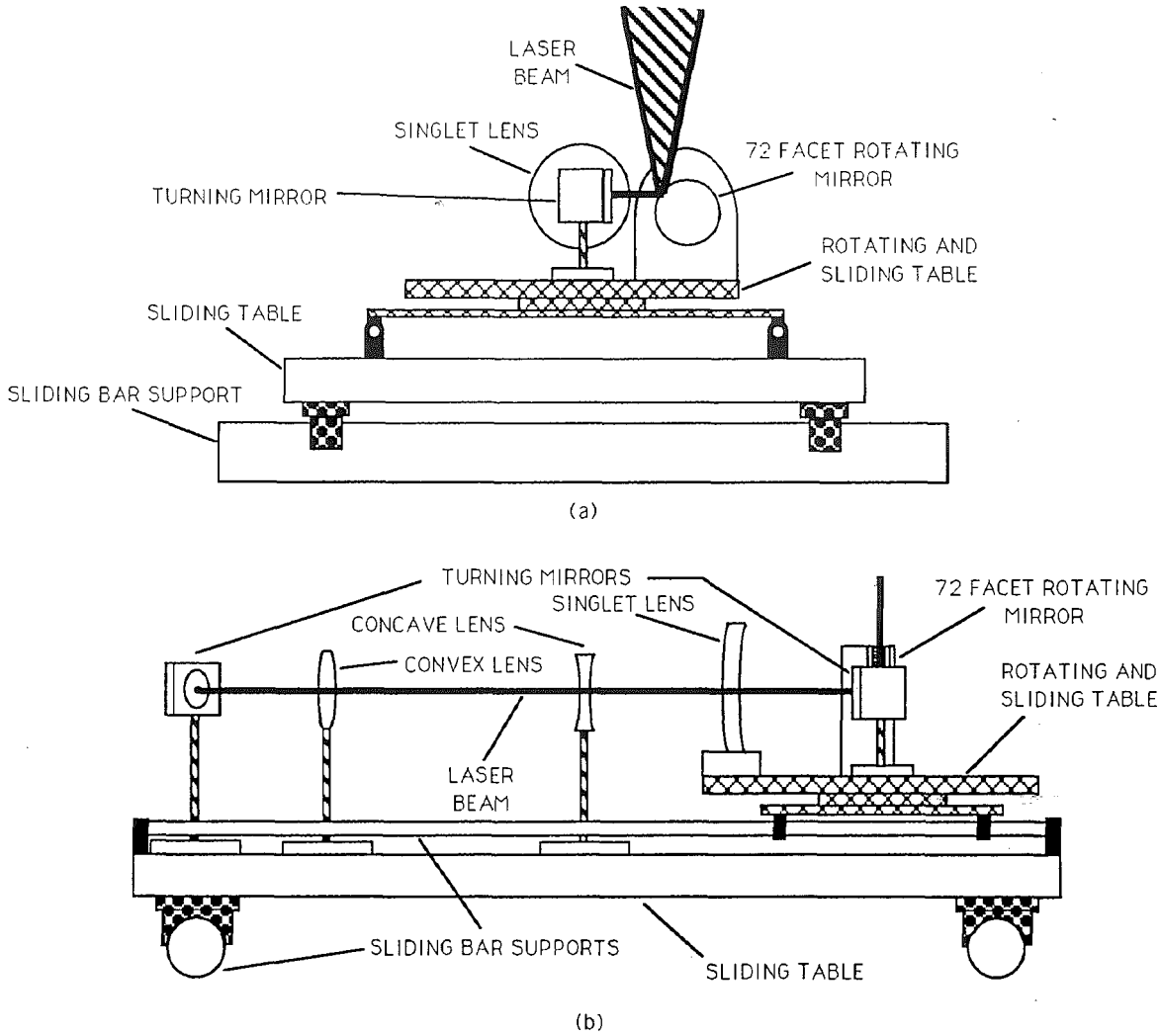

Figure 2.8: (a) End; and (b) side views of the rotating mirror and laser systems.

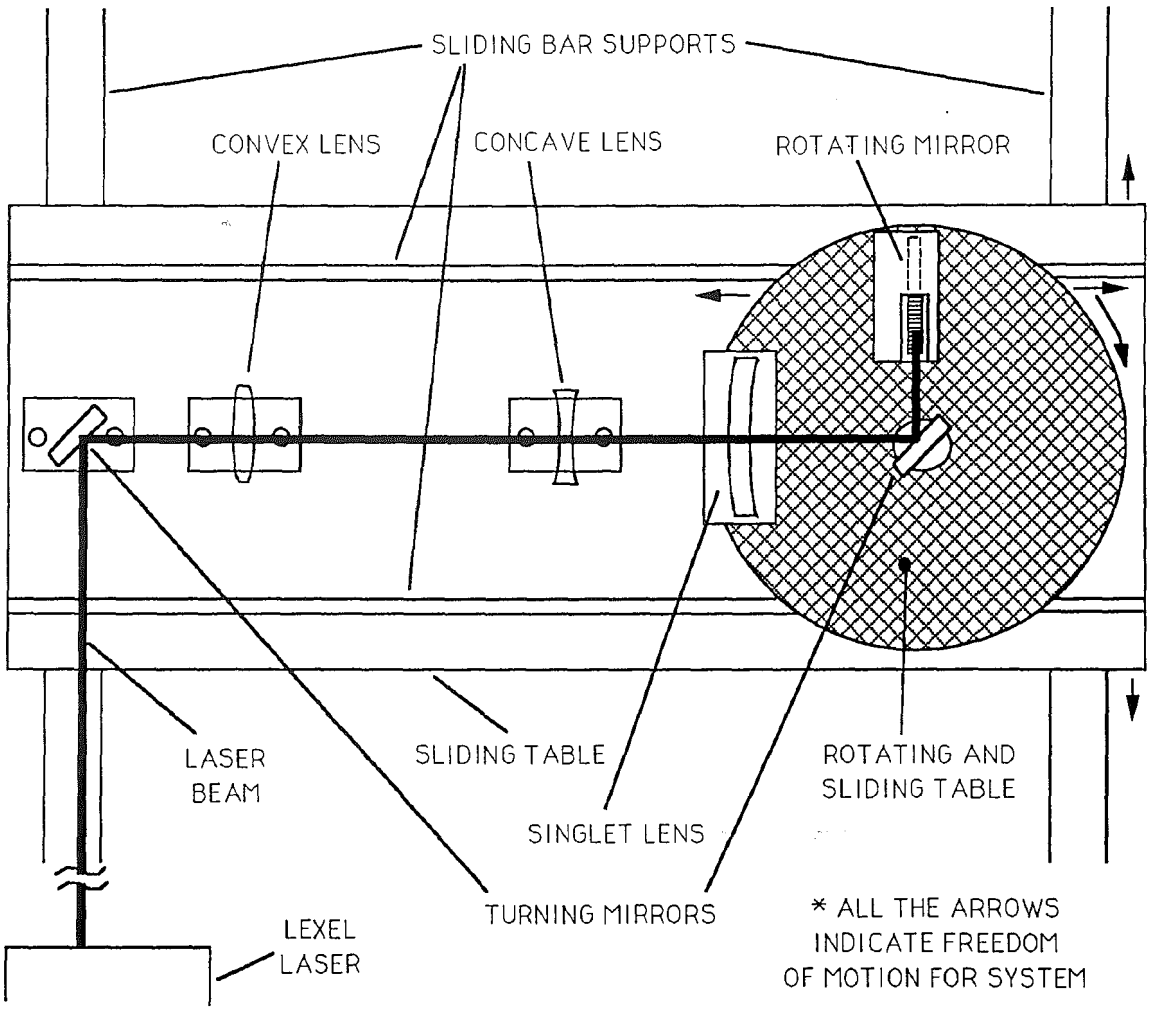

Figure 2.9: Plan view of the rotating mirror and laser systems.

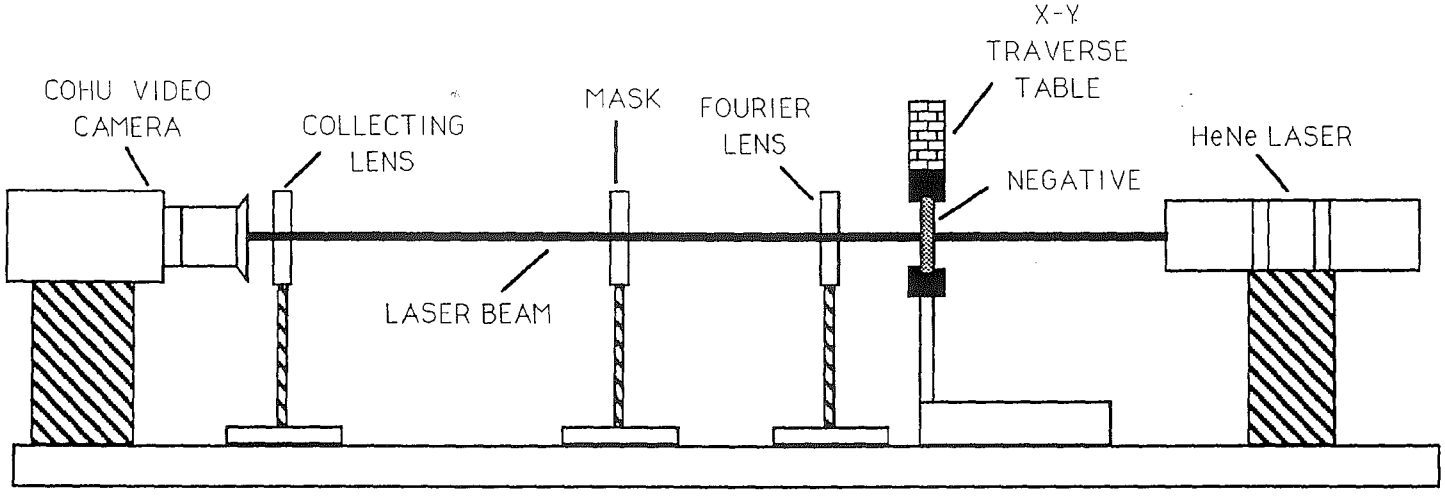

Figure 3.1: Particle Image Velocimetry (PIV) technique for interrogating a negative.

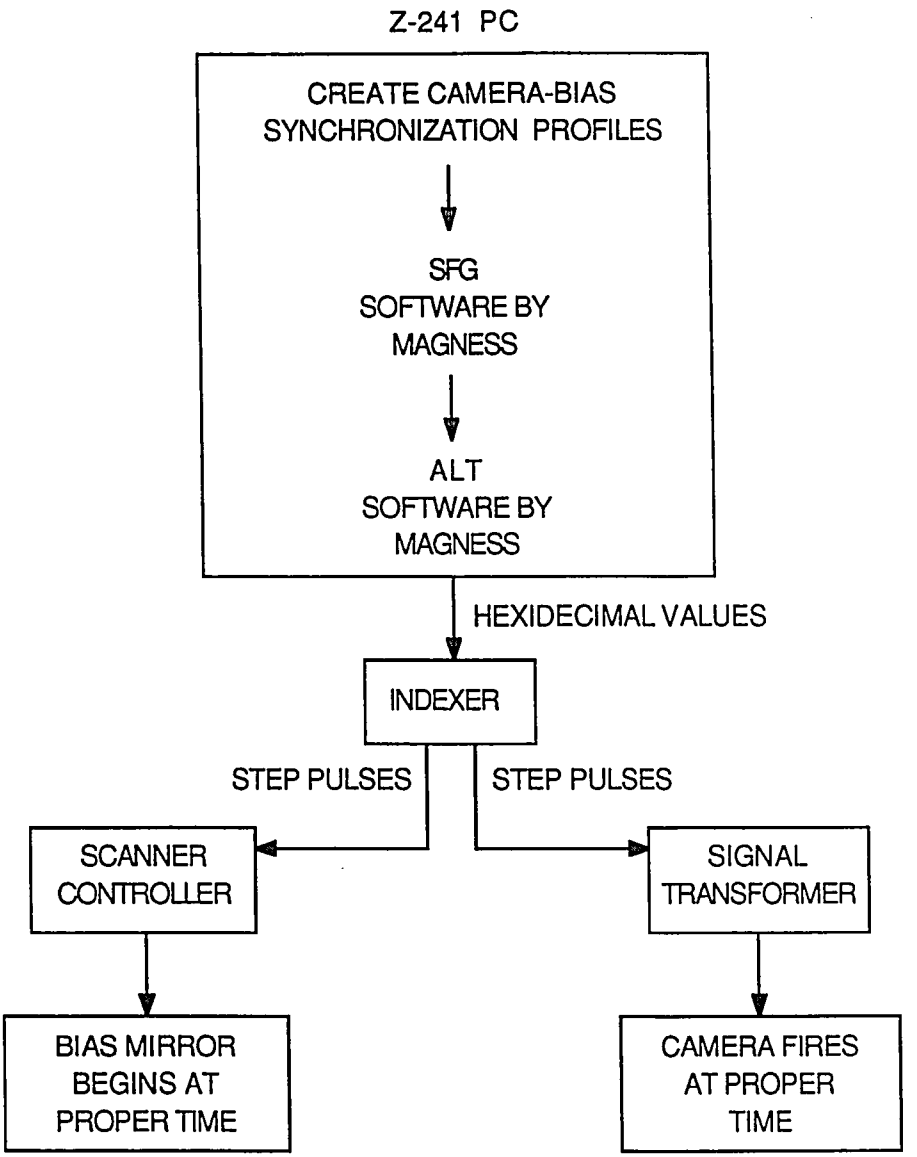

Figure 3.2: Schematic of the open-loop bias mirror and camera synchronization system.

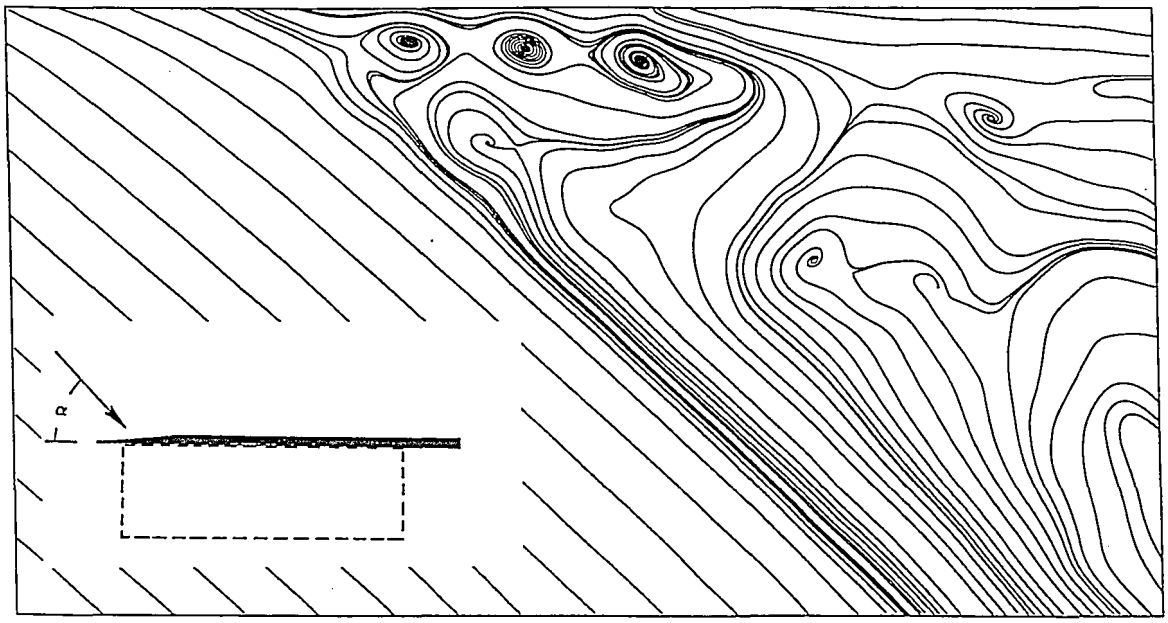

(a)

(b)

Figure 4.1: Instantaneous sectional streamline pattern over plane passing through the centerline of the leading-edge vortex portraying: (a) the helical instability mode and (b) a deviation from the helical instability mode of vortex breakdown for a stationary wing at an angle of attack, $\alpha = 40°$. Left and right sides of image correspond to distances from apex of wing of X/C = 0.08 and 0.96, respectively.

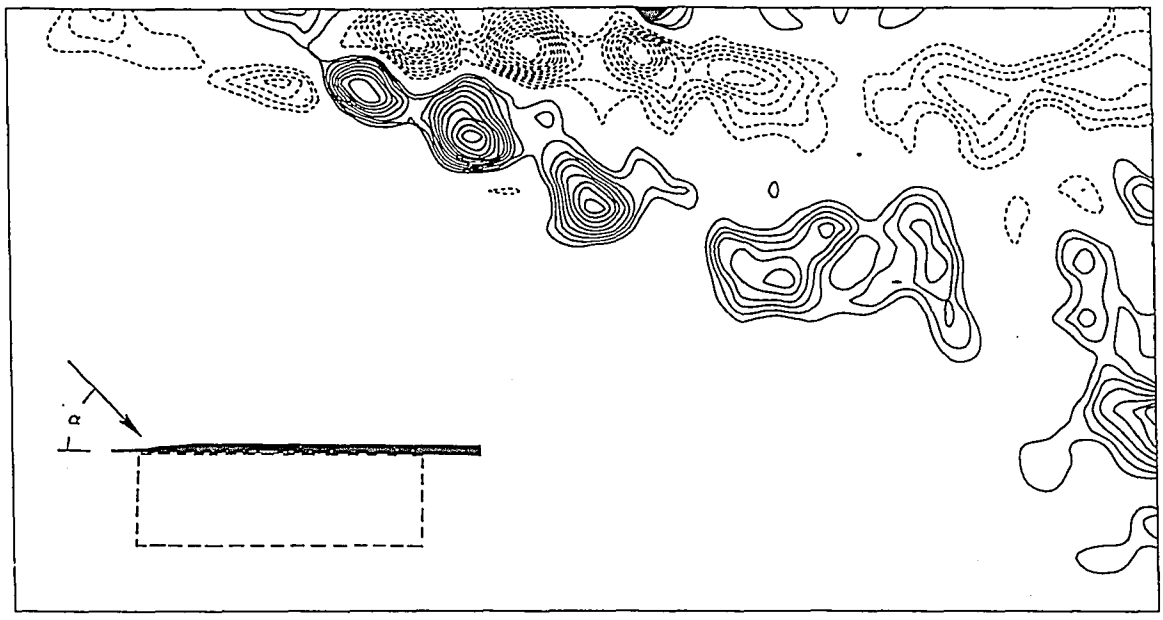

(a)

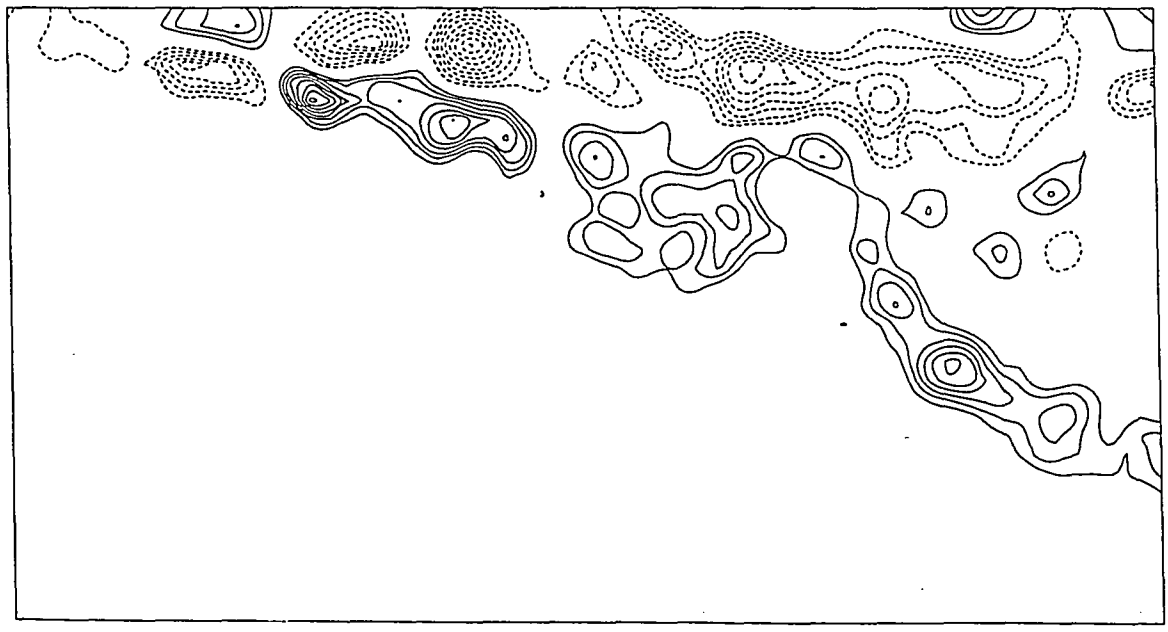

(b)

Figure 4.2: Contours of constant positive (solid line) and negative (dashed line) vorticity over a plane passing through the centerline of the leading-edge vortex portraying: (a) the helical instability mode and (b) a deviation of the helical instability mode of vortex breakdown for a stationary wing at an angle of attack, $\alpha = 40°$. Left and right sides of image correspond to distances from apex of wing of X/C = 0.08 and 0.96, respectively.

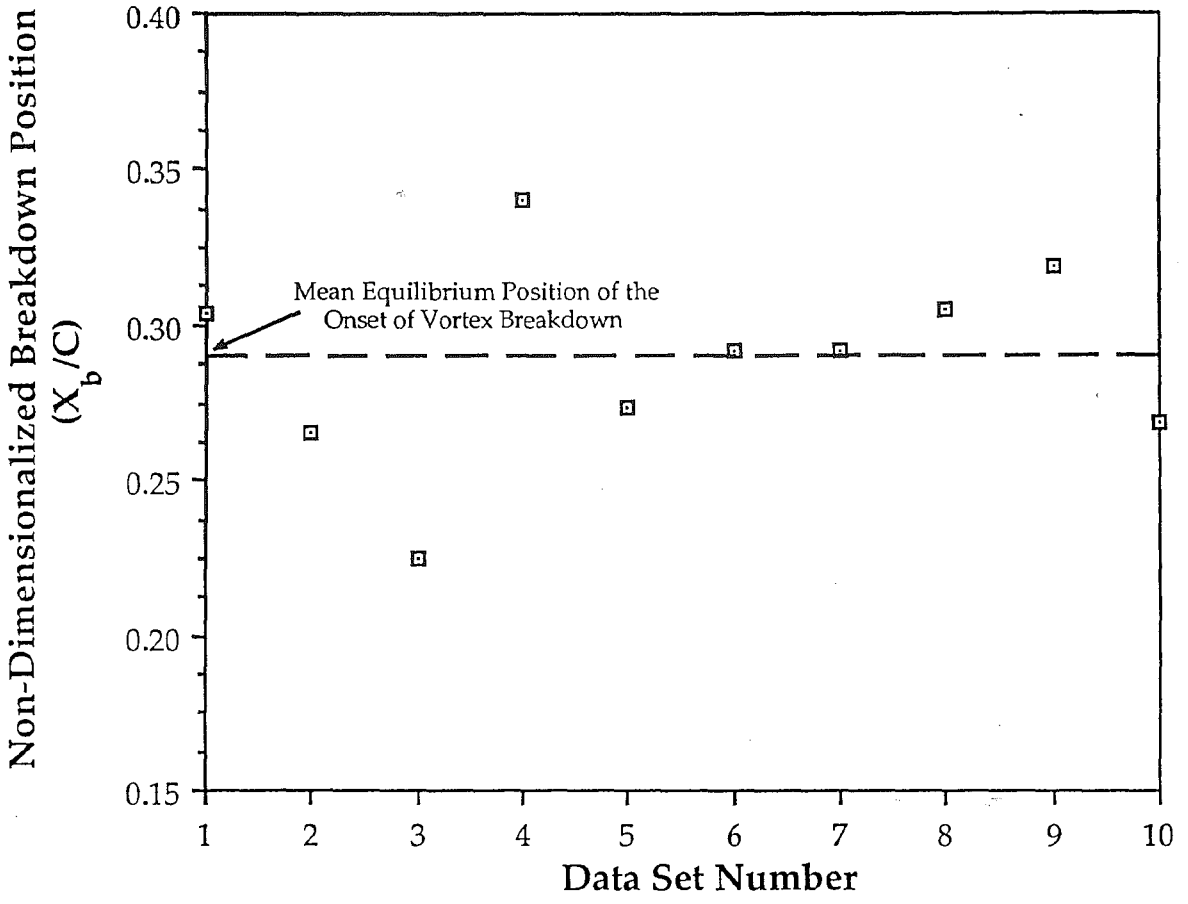

Figure 4.3: Plot of the location of the onset of vortex breakdown along the chord of the delta wing referenced from the apex for all ten cases in the first experiment in which the onset of breakdown has stabalized around a mean equilibrium position.

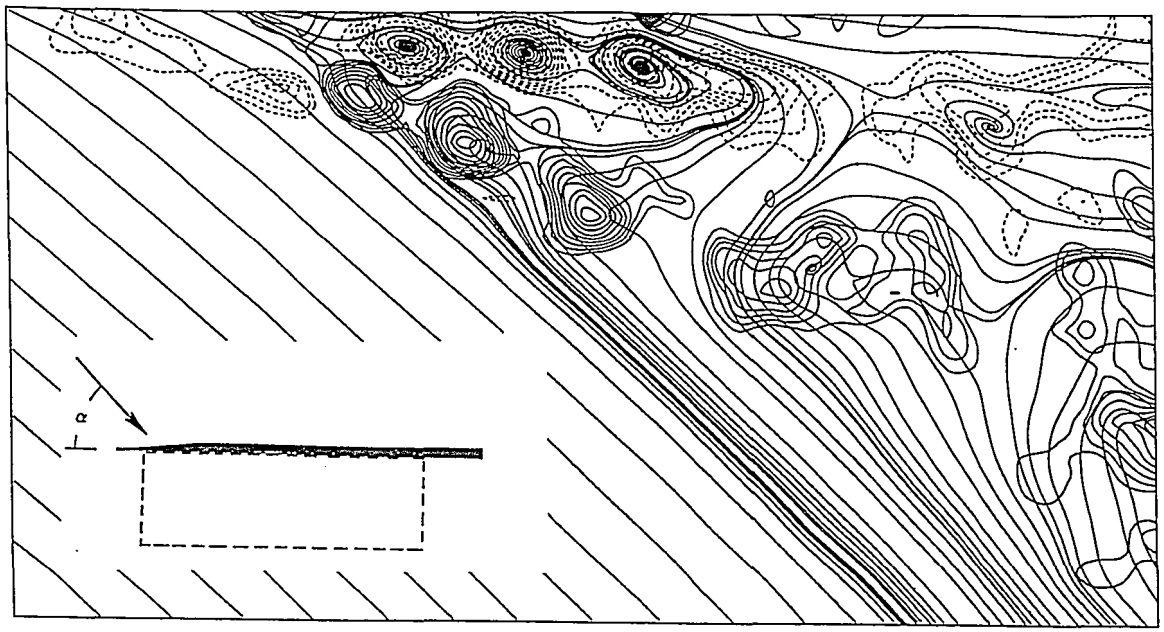

(a)

(b)

Figure 4.4: Superposition of contours of constant vorticity and corresponding sectional streamline patterns over a plane passing through the centerline of the leading-edge vortex portraying: (a) the helical instability mode and (b) a deviation of the helical instability mode of vortex breakdown for a stationary wing at an angle of attack, $\alpha = 40°$. Left and right sides of image correspond to distances from apex of wing of X/C = 0.08 and 0.96, respectively.

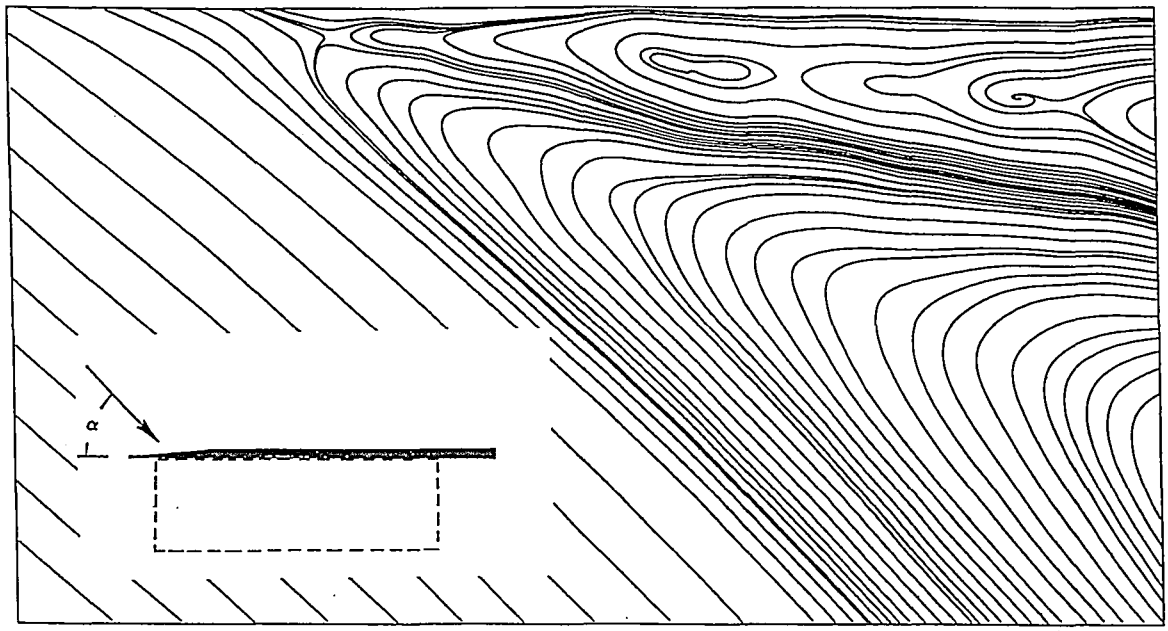

(a)

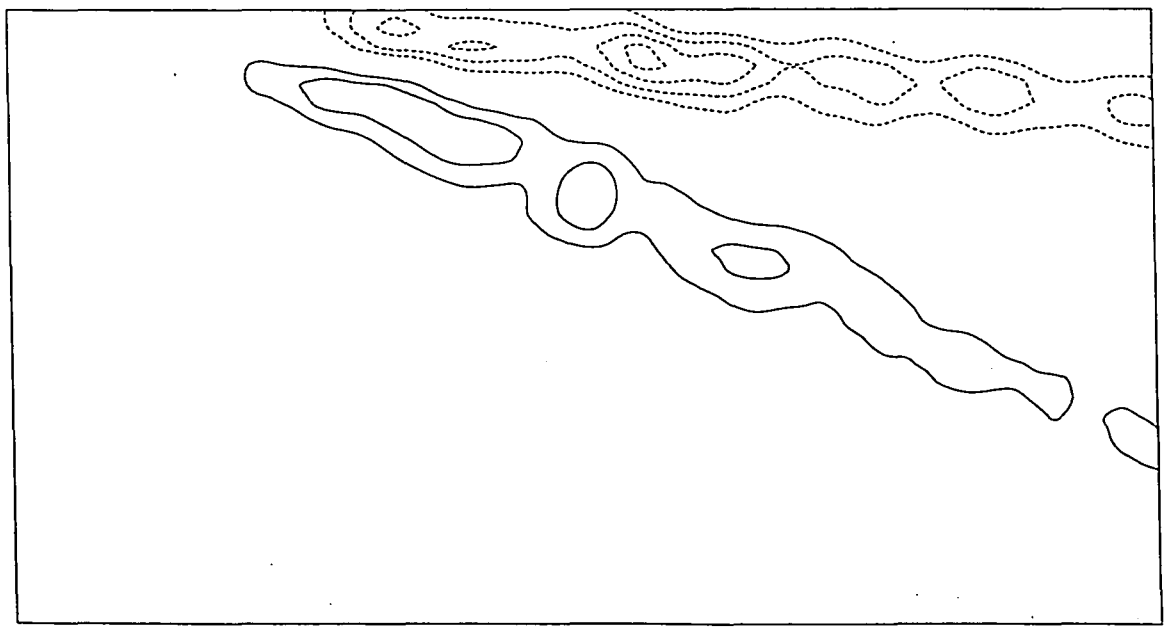

(b)

Figure 4.5: An average of the ten instantaneous velocity fields of vortex breakdown for a stationary wing at an angle of attack, α = 40°, and the corresponding (a) sectional streamline pattern and (b) contours of constant vorticity. Left and right sides of image correspond to distances from apex of wing of X/C = 0.08 and 0.96, respectively.

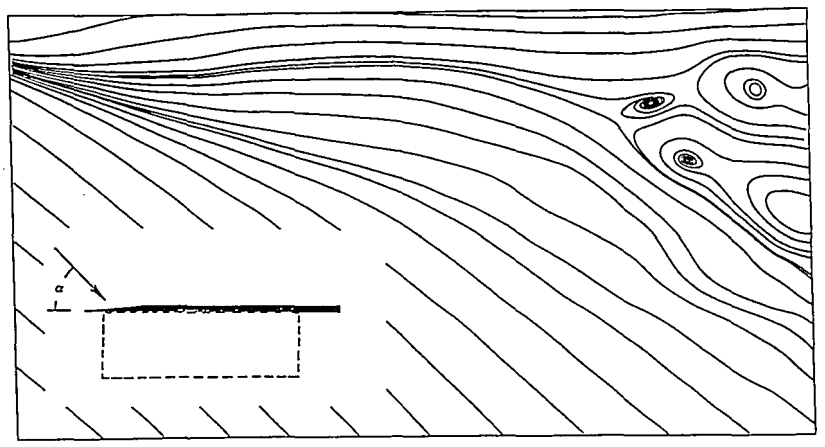

(a)

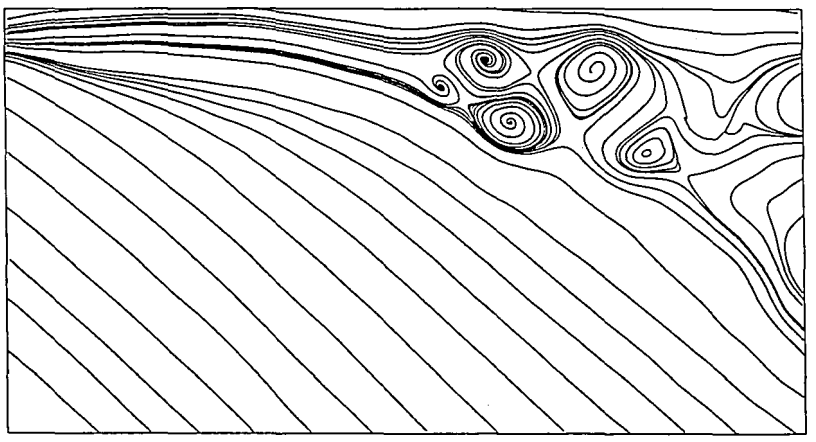

(b)

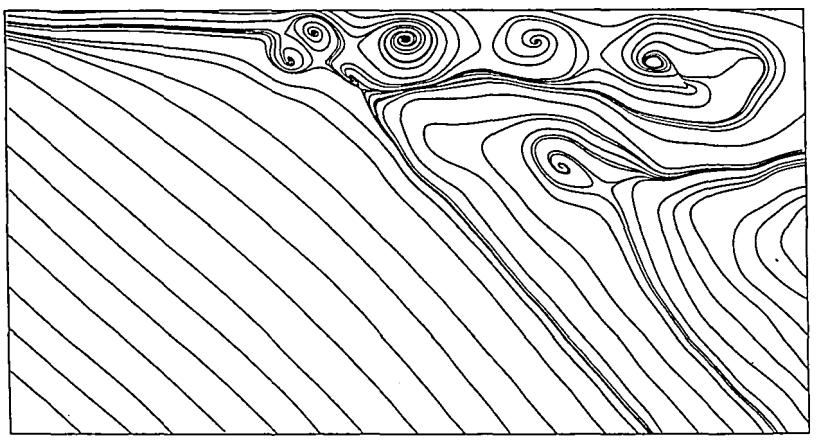

(c)

Figure 4.6: Instantaneous sectional streamline pattern over plane passing through the centerline of the leading-edge vortex at: (a) dimensionless time $t^* = tU/C = 0.41$; (b) $t^* = 0.83$; and (c) $t^* = 3.30$ after cessation of the pitching motion. Left and right sides of image correspond to distances from apex of wing of $X/C = 0.05$ and 0.93, respectively.

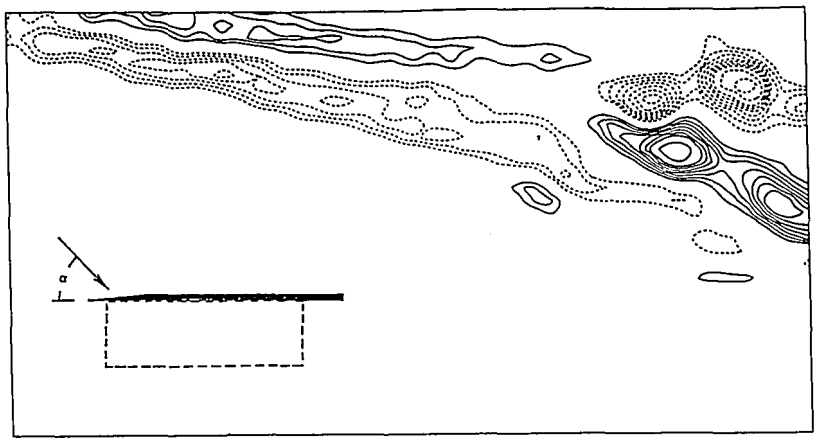

(a)

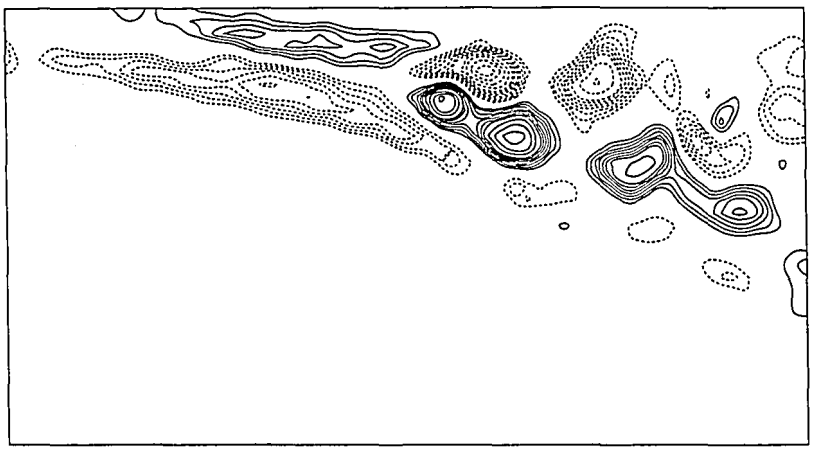

(b)

(c)

Figure 4.7: Contours of constant positive (solid line) and negative (dashed line) vorticity over a plane passing through the centerline of the leading-edge vortex at: (a) dimensionless time $t^* = tU/C = 0.41$; (b) $t^* = 0.83$; and (c) $t^* = 3.30$ after cessation of pitching motion. Left and right sides of image correspond to distances from apex of wing of $X/C = 0.05$ and 0.93, respectively.

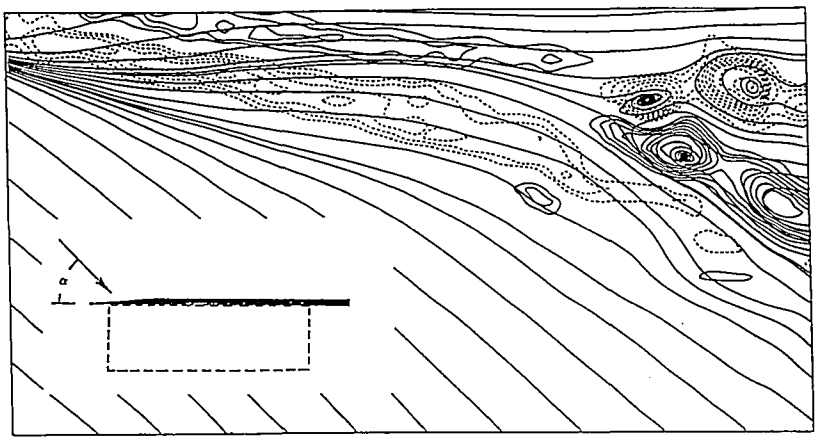

(a)

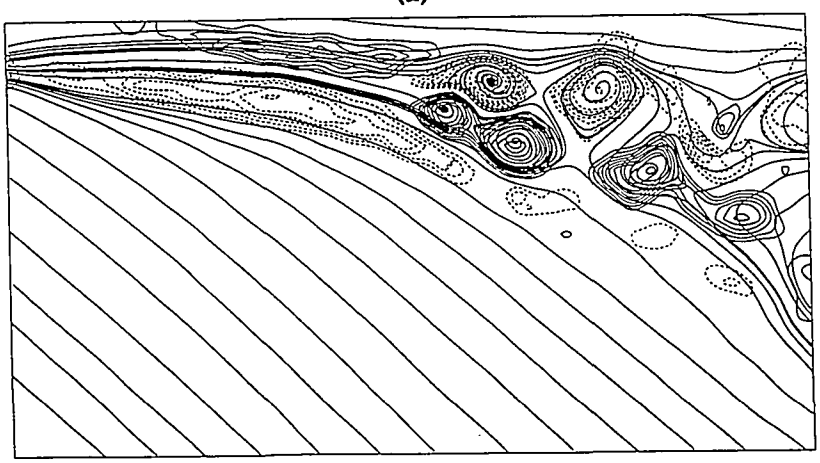

(b)

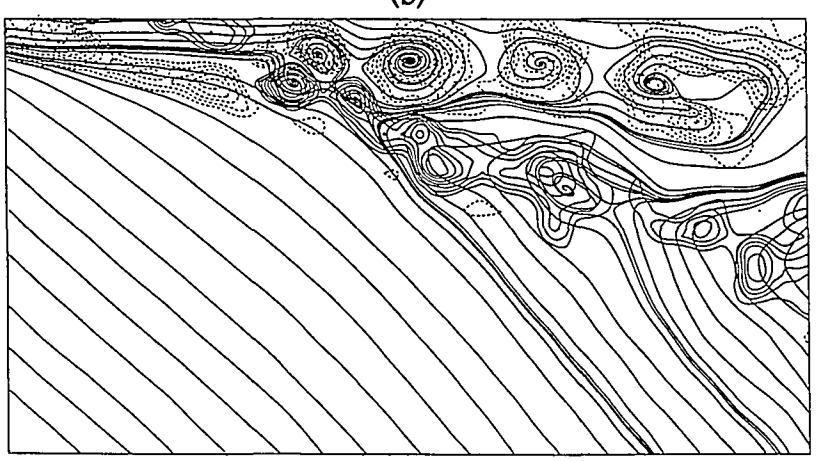

(c)

Figure 4.8: Superposition of contours of constant vorticity and corresponding sectional streamline patterns over a plane passing through the centerline of the leading-edge vortex at: (a) dimensionless time $t^* = tU/C = 0.41$; (b) $t^* = 0.83$; and (c) $t^* = 3.30$ after cessation of pitching motion. Left and right sides of image correspond to distances from apex of wing of $X/C = 0.05$ and 0.93, respectively.

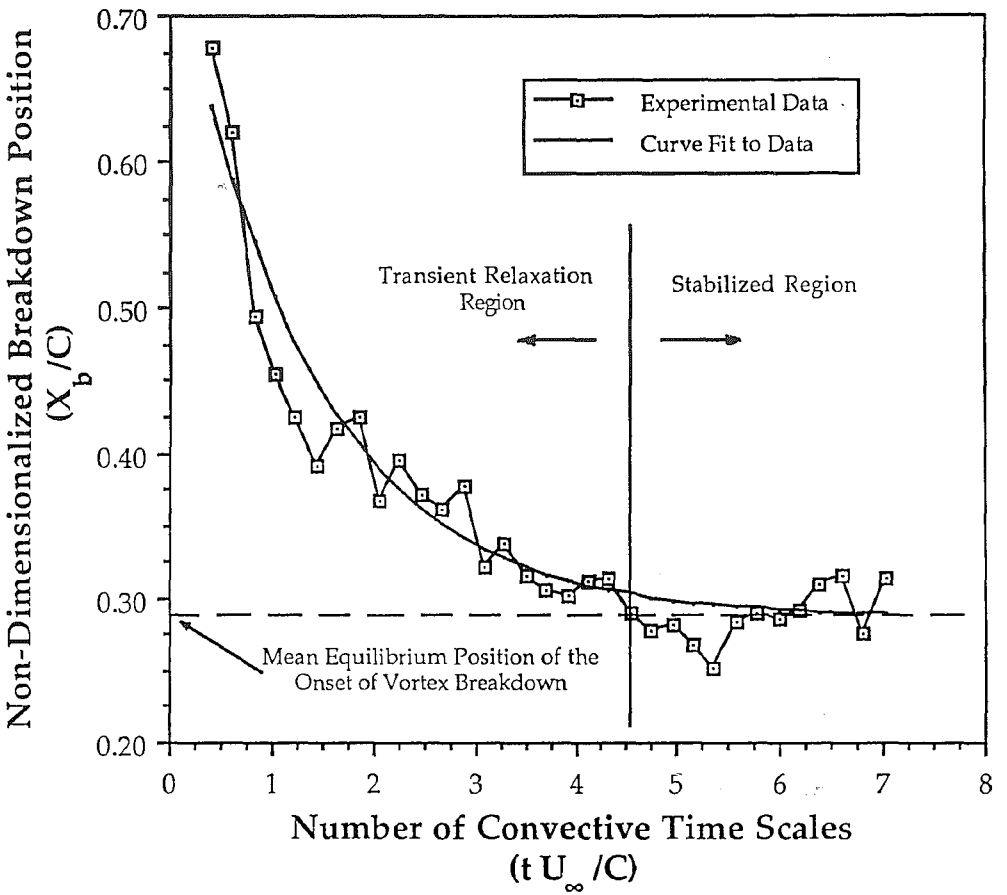

Figure 4.9: Plot of the location of the onset of vortex breakdown along the chord of the delta wing referenced from the apex for all thirty-three cases in the second experiment in which the onset of breakdown progresses towards and eventually stabilizes at the mean equilibrium position during the transient relaxation process after cessation of pitching motion.

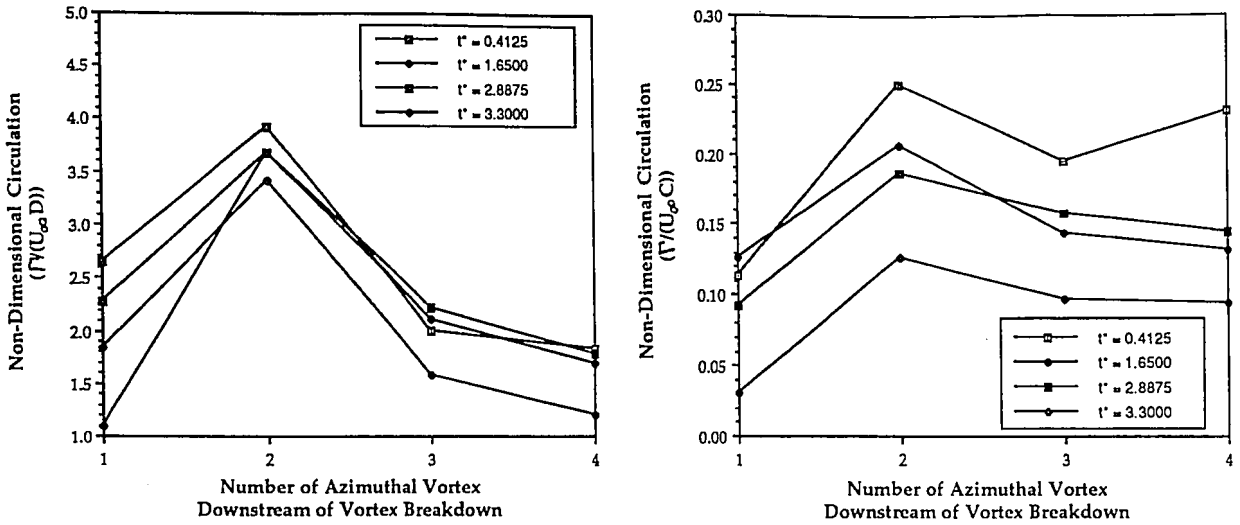

(a)

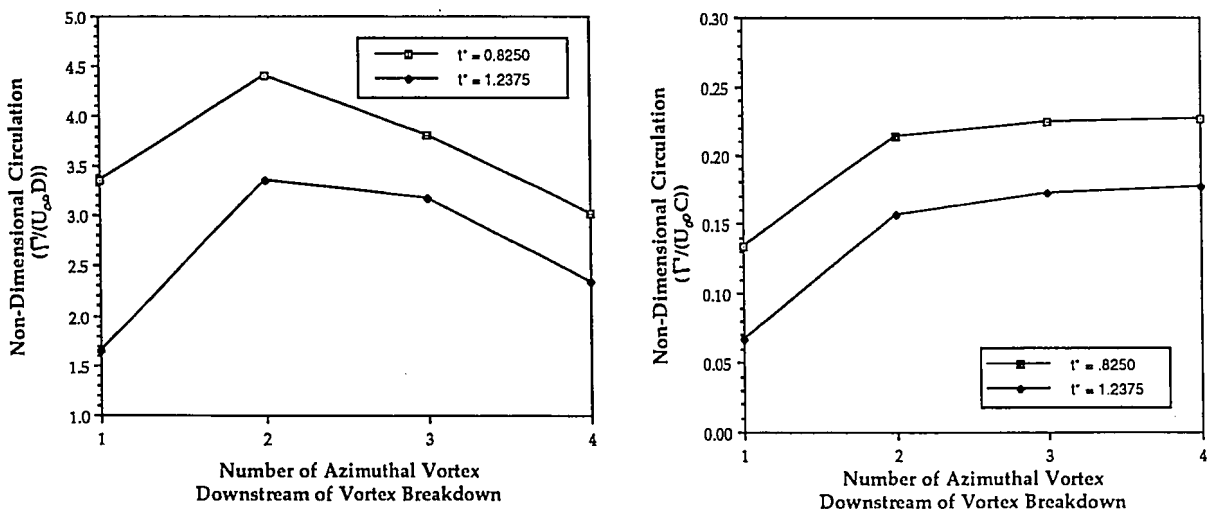

(b)

Figure 4.10: Plots of the absolute values of the non-dimensional circulation for the first four concentrations of vorticity downstream of the onset of vortex breakdown for the helical instability mode cases, when the signs of the vorticity clusters in order from first to last are: (a) negative, positive, negative, positive, and (b) positive, negative, positive, negative. The left plot in each section contains non-dimensional circulation, in which the characteristic length scale is based on the varying diameter of the core of vortex breakdown, where as in the right plot it is based on the chord length.

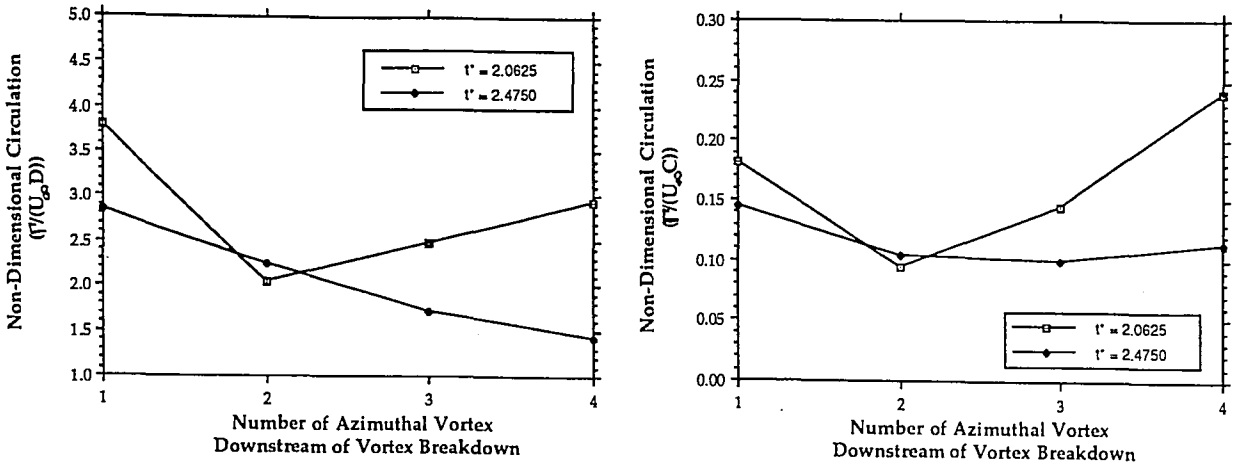

(a)

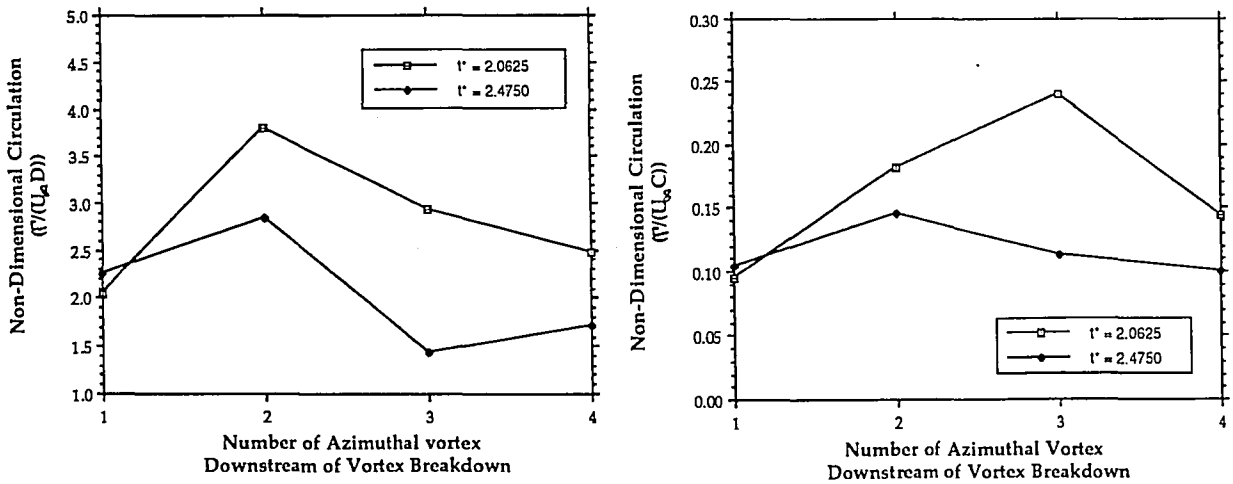

(b)

Figure 4.11: Plots of the absolute values of the non-dimensional circulation for the first four concentrations of vorticity downstream of the onset of vortex breakdown for the two cases, which deviated from the helical instability mode cases, assuming the signs of the vorticity clusters in order from first to last are: (a) negative, positive, negative, positive, and (b) positive, negative, positive, negative. The left plot in each section contains non-dimensional circulation, in which the characteristic length scale is based on the varying diameter of the core of vortex breakdown, where as in the right plot it is based on the chord length.

VITA

Joseph Towfighi was born November 27, 1966 in Camden, New Jersey to parents Javad and Judith M. Towfighi. After graduating from Camden Catholic High School in June, 1985, the author began undergraduate studies in mechanical engineering at Drexel University in Philadelphia, Pennsylvania. During this period he participated in a work study program, which resulted in three years of work experience in the area of missile research and development at Dyna East Corporation in Philadelphia, Pennsylvania. In June, 1990, he graduated magna cum laude with his Bachelor of Science Degree in Mechanical Engineering, and chose to continue his studies in mechanical engineering at Lehigh University in Bethlehem, Pennsylvania as a research assistant. In November, 1992, the author received his Master of Science Degree in Mechanical Enginnering, and is presently planning on furthering his work experience.

END

OF

TITLE